

Separability Analysis of Random FM Radar Waveforms

Matthew B. Heintzelman[✉], Member, IEEE, Daniel B. Herr, Member, IEEE, Charles A. Mohr[✉], Member, IEEE, Shannon D. Blunt[✉], Fellow, IEEE, Cenk Sahin[✉], Member, IEEE, and Andrew Kordik

Abstract—This work seeks to elucidate the relationship between interfering frequency-modulated (FM) radar waveforms and their observed separability. A statistical and analytical framework is developed through which the average separability is determined as a function of the mutual time–bandwidth product between the interfering waveforms. The analytically derived predictor for waveform separability is then compared to a long-observed heuristic. Since random waveforms exhibit stochastic cross correlations, the maximum deviation above the analytically derived predictor is also examined. High-dimensional Monte Carlo simulations are used to numerically validate the analytical results.

Index Terms—Multiple-input-multiple-output (MIMO) radar, multistatic radar, noise waveforms, waveform diversity.

I. INTRODUCTION

IT HAS been observed that the cross correlation between two interfering waveforms is dependent on three primary factors: 1) their relative power levels; 2) the degrees of freedom (DoFs) possessed by the waveforms; and 3) the common alignment of those DoFs. The common dimensionality alignment is characterized by their overlapping temporal and spectral support [1], [2]. For instance, two radars may alternate operations in a time-division manner to achieve perfect isolation [3], [4]. With sufficient front-end filtering, essentially the same result can also be achieved via frequency division given enough spectral separation and containment [5], [6]. In other words, those cases imply zero common dimensionality in time or frequency.

In general, one can define the common dimensionality for two radars in terms of the mutual time–bandwidth product, which is simply the product of the temporal support and

Received 2 December 2024; revised 19 March 2025; accepted 11 April 2025. Date of publication 24 April 2025; date of current version 29 May 2025. This work was supported by the Air Force Research Laboratory (AFRL) through a subcontract with Defense Engineering Corporation for research under Prime Contract FA8650-20-C-1955. Distribution Statement A. Approved for Public Release. (*Corresponding author:* Matthew B. Heintzelman.)

Matthew B. Heintzelman, Daniel B. Herr, and Shannon D. Blunt are with the Radar Systems Laboratory (RSL), University of Kansas (KU), Lawrence, KS 66045 USA (e-mail: mheintzelman1@ku.edu; d110h720@ku.edu; sdblunt@ku.edu).

Charles A. Mohr is with the Radar Systems Laboratory (RSL), University of Kansas (KU), Lawrence, KS 66045 USA (e-mail: charles.mohr@ku.edu).

Cenk Sahin is with Johns Hopkins Applied Physics Laboratory, Laurel, MD 20723 USA (e-mail: Cenk.Sahin@jhuapl.edu).

Andrew Kordik is with the AFRL Sensors Directorate, Wright-Patterson AFB, Dayton, OH 45433 USA (e-mail: andrew.kordik.1@us.af.mil).

Digital Object Identifier 10.1109/TRS.2025.3564236

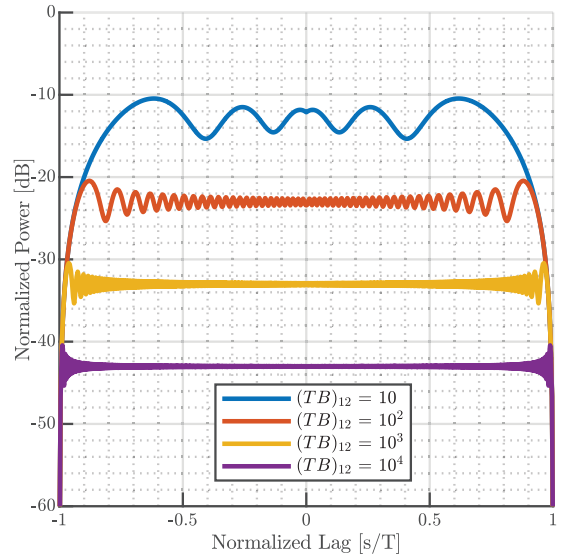


Fig. 1. Upchirp/downchirp cross correlations as a function of mutual time–bandwidth product.

spectral support that the radars share. Intuitively, it is this mutual time–bandwidth product that ultimately determines the separability between distinct radar waveforms. The purpose of this article is to provide mathematical rigor to this notion.

First, consider the well-known energy-normalized cross correlation between two waveforms $s_1(t)$ and $s_2(t)$ that have mutual time–bandwidth product denoted as $(\text{TB})_{12}$ to distinguish from the traditional single-waveform time–bandwidth product TB. The normalized cross correlation is given by

$$c_{1,2}(\tau) = \frac{1}{\sqrt{E_1 E_2}} \int_{-\infty}^{\infty} s_1^*(t - \tau) s_2(t) dt \quad (1)$$

for signal energies E_1 and E_2 . The result in (1) describes the particular interference that the presence of $s_1(t)$ and $s_2(t)$ imposes upon one another when matched filtering for one of them is performed.

For example, upchirp and downchirp linear frequency modulation (LFM) waveforms provide a useful baseline case. Fig. 1 illustrates their cross correlation for different $(\text{TB})_{12}$ values (here with complete overlap). Specifically, each pair has the same pulsedwidth and equal but opposite chirp rates to yield the same bandwidth. We observe that increasing $(\text{TB})_{12}$ by factors of 10× corresponds to a 10× reduction in the

peak correlation value (determined by the edge ripples), which occurs at approximately $-10\log_{10}(0.9(TB)_{12})$. This result is derived explicitly in Appendix A, where (1) is computed for the case of interfering chirp waveforms. Unsurprisingly, this result implies that increasing the shared dimensionality can provide improved separability, with the caveat that the waveforms are distinctly different.

In the case of upchirp/downchirp, it is also worth noting that the cross correlation process involves only a single instantaneous point of time–frequency overlap for any lag value τ . Recalling how the principle of stationary phase [7] relates chirp rate to a waveform’s energy-per-unit frequency, these $10\times$ higher chirp rates also suggest a proportionally lower instantaneous spectral overlap between the upchirp and downchirp. While this perspective aids in our understanding of separability between LFM waveforms, the relationship is generally more complicated when addressing diverse waveforms.

Previous work has examined the impact of separability on phase codes and discrete sequences [8], [9], [10], [11], providing analytical bounds on the achievable minimum cross correlation for such signals. The design of so-called “orthogonal” and low-correlation phase codes for use in code-division radar systems has also been examined [12], [13], [14], [15], [16], [17]. However, since most radars operate a high-power amplifier in saturation, unwanted amplitude modulation arises when abrupt phase transitions occur [18], [19], resulting in transmitter distortion that can hinder the utility of phase codes in practice. Consequently, we herein explore separability in the context of frequency-modulated (FM) waveforms because their constant-amplitude/continuous-phase structure conforms to the requirements of high-power amplification.

Now, consider the cross correlation between two interfering random FM (RFM) waveforms, a wide variety of which have been experimentally demonstrated in hardware to be appropriate for high-power radar applications and can provide high dimensionality (see [20] and references therein). The candidate waveforms here are unoptimized first-order polyphase-code FM (PCFM) [18] having complete overlap in temporal and spectral support. Since these waveforms are independent instantiations of a random process (here a uniform distribution on $[-\pi, +\pi]$ for each underlying code element), it becomes necessary to examine their cross correlation via Monte Carlo simulation, with rigorous analysis to follow in later sections.

For the same $10\times$ increment factors in mutual time–bandwidth product, a randomly generated ensemble of 200 independent waveforms was realized at each level, providing 100 cross correlation responses. Each set of cross correlation responses was then root mean square (rms) averaged to obtain a measure of per-pulse behavior. The results are depicted in Fig. 2, which echoes the observations from Fig. 1: i.e., mutual time–bandwidth is the driving factor in the separability of independent waveforms. It is also noteworthy that the zero-lag cross correlation level in Fig. 2 is likewise approximately $-10\log_{10}[(TB)_{12}]$, a fact that is explored further in Section II.

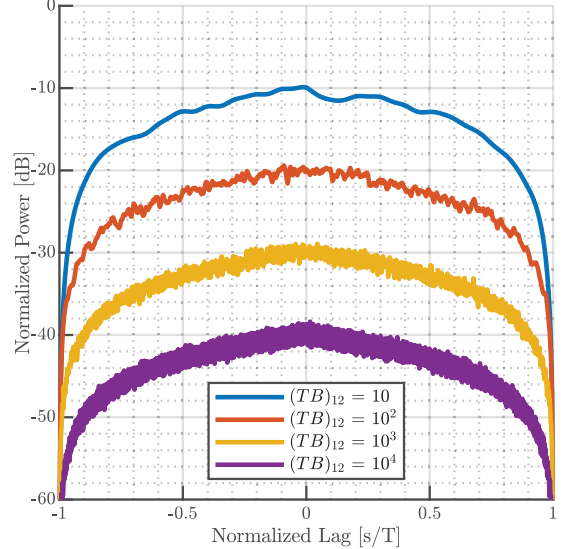


Fig. 2. RMS-averaged cross correlation over 100 pairs of independent RFM waveforms as a function of mutual time–bandwidth product.

Using these separability observations as a guide, this article analytically derives the expected cross correlation for independent instantiations of RFM waveforms, confirming this analysis with Monte Carlo simulations. The notion of a multistatic interference floor is then explored to establish how the distribution of scattering impacts separability. Finally, in addition to the mean cross correlation, the maximum cross correlation is analytically derived since this attribute affects false alarms in the radar detection stage.

II. EXPECTED CROSS CORRELATION

We wish to evaluate the expected value of the squared magnitude of the normalized cross correlation [given by (1)] between two independent RFM waveforms $s_1(t)$ and $s_2(t)$ that have constant envelope and continuous phase. For simplicity, assume that both waveforms have time support on $t \in [0, T]$, though that need not be the case in general. The following demonstrates that the primary factor in determining the cross correlation between random waveforms is their degree of overlapping temporal and spectral support.

Throughout this section, the zero-lag value of the cross correlation $c_{1,2}(\tau)$ is used as a reasonable overestimation of the average cross correlation level, which is visually confirmed by examining the peaks in Fig. 2. For further justification of this approximation, consider the expected power in the cross correlation, which from (1) is computed as

$$\begin{aligned} & E \left\{ |c_{1,2}(\tau)|^2 \right\} \\ &= E \left\{ \left| \frac{1}{\sqrt{E_1 E_2}} \int_{-\infty}^{\infty} s_1^*(t - \tau) s_2(t) dt \right|^2 \right\} \\ &= \frac{1}{E_1 E_2} E \left\{ \left(\int_{-\infty}^{\infty} s_1^*(t_1 - \tau) s_2(t_1) dt_1 \right)^* \times \left(\int_{-\infty}^{\infty} s_1^*(t_2 - \tau) s_2(t_2) dt_2 \right) \right\} \end{aligned}$$

$$= \frac{1}{E_1 E_2} E \left\{ \int_{-\infty}^{\infty} \int_{-\infty}^{\infty} \left(\begin{array}{c} s_1^*(t_1 - \tau) s_2(t_1) \\ \times s_1(t_2 - \tau) s_2^*(t_2) \end{array} \right) dt_1 dt_2 \right\} \quad (2)$$

where $E\{\cdot\}$ is the expectation operator. Rearranging terms and passing the expectation through the time integrations via Fubini's theorem, (2) then becomes

$$\begin{aligned} & E \left\{ |c_{1,2}(\tau)|^2 \right\} \\ &= \frac{1}{E_1 E_2} \int_{-\infty}^{\infty} \int_{-\infty}^{\infty} E \left\{ \begin{array}{c} s_1^*(t_1 - \tau) s_1^*(t_2 - \tau) \\ \times s_2(t_1) s_2^*(t_2) \end{array} \right\} dt_1 dt_2. \end{aligned} \quad (3)$$

Based on the assumption of statistical independence between processes $s_1(t)$ and $s_2(t)$, we can invoke multiplicative separability of the expected value as

$$\begin{aligned} E \left\{ \begin{array}{c} s_1^*(t_1 - \tau) s_1(t_2 - \tau) \\ \times s_2(t_1) s_2^*(t_2) \end{array} \right\} &= E \left\{ s_1^*(t_1 - \tau) s_1(t_2 - \tau) \right\} \\ &\quad \times E \left\{ s_2(t_1) s_2^*(t_2) \right\} \\ &= R_{11}^*(t_1 - \tau, t_2 - \tau) \\ &\quad \times R_{22}(t_1, t_2) \end{aligned} \quad (4)$$

where $R_{11}(t_1, t_2)$ and $R_{22}(t_1, t_2)$ are the statistical autocorrelations of $s_1(t)$ and $s_2(t)$, respectively. Substituting this expression into (3) produces

$$\begin{aligned} E \left\{ |c_{1,2}(\tau)|^2 \right\} &= \frac{1}{E_1 E_2} \int_{-\infty}^{\infty} \int_{-\infty}^{\infty} \left[\begin{array}{c} R_{11}^*(t_1 - \tau, t_2 - \tau) \\ \times R_{22}(t_1, t_2) \end{array} \right] dt_1 dt_2 \\ &= \frac{1}{E_1 E_2} \langle R_{22}(t_1, t_2), R_{11}(t_1 - \tau, t_2 - \tau) \rangle_{t_1, t_2} \end{aligned} \quad (5)$$

where $\langle \cdot \rangle_{t_1, t_2}$ indicates the 2-D inner product performed over t_1 and t_2 , with (5) expressing the expected power of the cross correlation as the 2-D inner product between the statistical autocorrelations for the two independent waveforms. Intuitively, this result is greatest when there is maximum overlap between the autocorrelation main lobes, which has also been observed in simulation, as indicated in Fig. 2. This result implies that, on average, $\tau = 0$ is the lag at which the maximum expected correlation occurs.

Since $s_1(t)$ and $s_2(t)$ are statistically independent and have finite time extent, the zero-lag value should therefore provide a reasonable estimate of the average response for peak cross correlation level. Now, consider the expected power of the normalized cross correlation at zero lag, denoted as

$$\begin{aligned} \mu_0^2 &= E \left\{ |c_{1,2}(0)|^2 \right\} \\ &= E \left\{ \left| \frac{1}{\sqrt{E_1 E_2}} \int_0^T s_1^*(t) s_2(t) dt \right|^2 \right\}. \end{aligned} \quad (6)$$

Based on (5), we can rewrite (6) as the inner product of the waveform autocorrelations via

$$\mu_0^2 = \frac{1}{E_1 E_2} \langle R_{22}(t_1, t_2), R_{11}(t_1, t_2) \rangle_{t_1, t_2} \quad (7)$$

for $t_1, t_2 \in [0, T]$. As shown in Appendix B, the conjugate symmetry of the autocorrelation function can simplify (7) as

$$\mu_0^2 = \frac{2}{E_1 E_2} \text{Re} \left\{ \int_0^T \int_0^{t_2} R_{11}^*(t_1, t_2) R_{22}(t_1, t_2) dt_1 dt_2 \right\} \quad (8)$$

where $\text{Re}\{\cdot\}$ indicates the real operator.

We can further simplify (8) by assuming that the instantaneous phase for each RFM waveform is a wide-sense stationary (WSS) random process. Under this assumption, we can state that the autocorrelations can be entirely determined by the relative lag between times t and τ . Therefore, (8) can be rewritten as

$$\begin{aligned} \mu_0^2 &= \frac{2}{E_1 E_2} \text{Re} \left\{ \int_0^T \int_0^{t_2} \left[\begin{array}{c} R_{11}^*(t_1 - t_2) \\ \times R_{22}(t_1 - t_2) \end{array} \right] dt_1 dt_2 \right\} \\ &= \frac{2}{E_1 E_2} \text{Re} \left\{ \int_0^T \int_0^v R_{11}^*(u) R_{22}(u) du dv \right\} \end{aligned} \quad (9)$$

where the substitution of variables $u = t_1 - t_2$ indicates integration over a relative lag parameter and the variable $v = t_2$ has been introduced for clarity. This form permits convenient numerical evaluation since the autocorrelations need only be computed over a single variable, meaning that, for WSS processes, the 2-D correlations become 1-D.

III. EVALUATION OF EXPECTED CROSS CORRELATION

To assess the efficacy of the expected cross correlation level in (9), we examine a variety of RFM waveform classes. Specifically, we consider first-order PCFM with random coding [18], [19], pulsed constant-envelope orthogonal frequency-division multiplexing (CE-OFDM) with random coding [21], [22], [23], random phase-codes [7], pseudorandom optimized FM (PRO-FM) with a super-Gaussian spectrum shaping of $n = 4$ [24], [25], and standard LFM (upchirp versus downchirp) as a benchmark. For the FM waveforms considered here, the waveform energies are computed as $E_1 = a_1^2 T$ and $E_2 = a_2^2 T$, where a_1 and a_2 are the amplitudes of waveforms 1 and 2, respectively.

It was observed in Figs. 1 and 2 that the inverse of the mutual time-bandwidth product (TB)₁₂ is a useful and simple estimate of the expected cross correlation between two waveforms. To be clear, the mutual time-bandwidth product refers to the multiplication of overlapping time and frequency support of the two interfering waveforms and corresponds to the common DoFs between them. Appendix C provides an analytical justification for this observation, with each autocorrelation approximated as a sinc function as a convenient surrogate that can be integrated in closed form. Per Appendix C, when the waveforms are perfectly overlapping in frequency, this approximation leads to

$$\mu_0^2 \approx \frac{1}{(\text{TB})_{12}} \quad (10)$$

which is exactly the inverse mutual time-bandwidth product.

In the following, μ_0^2 from (10) is compared with the expected cross correlation level from (9) via Monte Carlo simulation, thereby testing the efficacy of the inverse-TB rule of thumb. The evaluation is performed over an ensemble of cross correlations, generated from unique pulse pairs, for each class of FM waveforms described above. For completeness, a purely numerical estimate is also obtained using the rms cross correlation for each ensemble of waveforms as

$$\mu_{0,\text{rms}}^2 \approx \text{rms} \{ c_0(0), c_1(0), \dots, c_M(0) \} \quad (11)$$

where $c_m(0)$ is the zero-lag value of the m th cross correlation function from the ensemble of M independent assessments.

TABLE I
ZERO-LAG EXPECTED CROSS CORRELATION VALUES (TB = 85)

Waveform class	RMS average correlation (11)	Predicted correlation (9)
PCFM	-20.83 dB	-20.54 dB
CE-OFDM	-21.21 dB	-20.53 dB
Phase codes	-20.12 dB	-20.98 dB
PRO-FM	-20.73 dB	-20.37 dB
LFM up/down	-23.68 dB	-20.24 dB

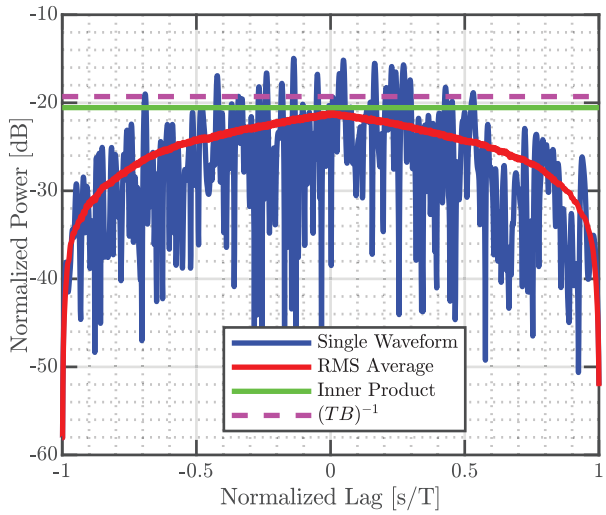


Fig. 3. Cross correlation for random 1st-order PCFM (TB = 85) compared to predictions of expected correlation.

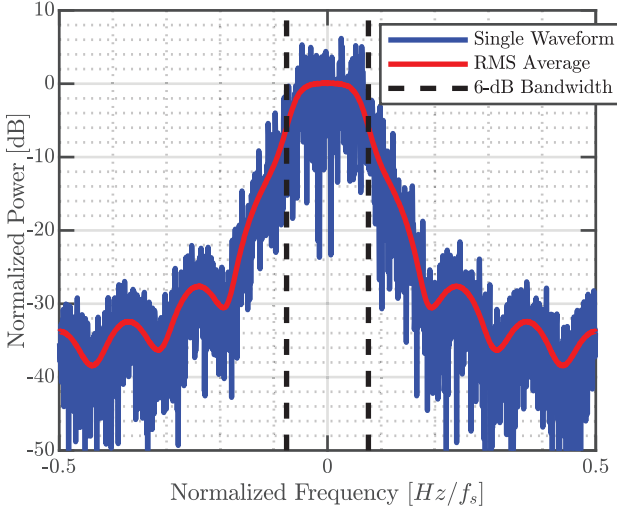


Fig. 4. PSD for random 1st-order PCFM (TB = 85).

A. Modest TB Case

First, consider a modest per-pulse waveform dimensionality of TB = 85, which is reasonable for moving target indication (MTI) applications. For each waveform class, 10000 cross correlation responses were generated from two unique sets of 10000 independent random waveforms. The predicted

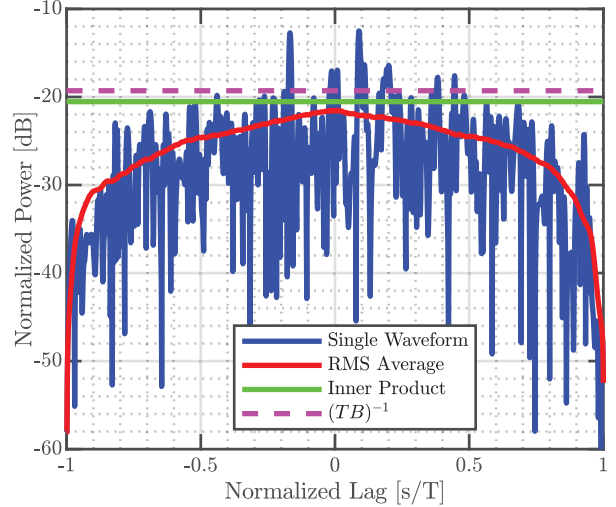


Fig. 5. Cross correlation for random CE-OFDM (TB = 85) compared to predictions of expected correlation.

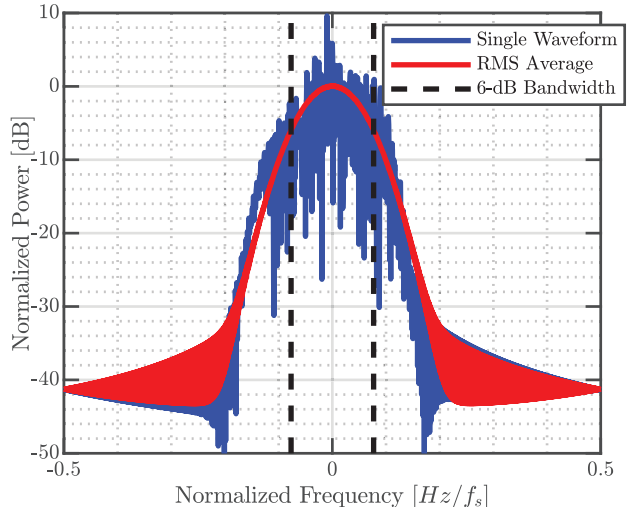


Fig. 6. PSD for random CE-OFDM (TB = 85).

correlation via (9) and the root-mean-square (rms) average correlation via (11) were then determined for each class, as listed in Table I. We observe that the numerical rms cross correlation values are within 0.7 dB of their predicted values for all four of the random waveform classes. The outlier is the cross correlation between upchirp/downchirp LFM waveforms, in which the numerical response is roughly 3 dB better than the prediction based on (9). The LFM case (and possibly other monotonic forms of nonlinear FM [27]) could be viewed as benchmarks on separability since their upchirp/downchirp versions only have a single crossing of instantaneous frequency versus time. For comparison, the inverse-TB heuristic from (10) yields $-10 \log_{10} (\text{TB}) = 19.3$ dB.

Figs. 3–7 depict the different measures of cross correlation assessed for the four random waveform classes along with LFM, while Figs. 8–12 illustrate the corresponding power spectral density (PSD) for each class. Noting that the spectral shape for random phase codes is determined by chip width, meaning that the normalized rms bandwidth is fixed for a

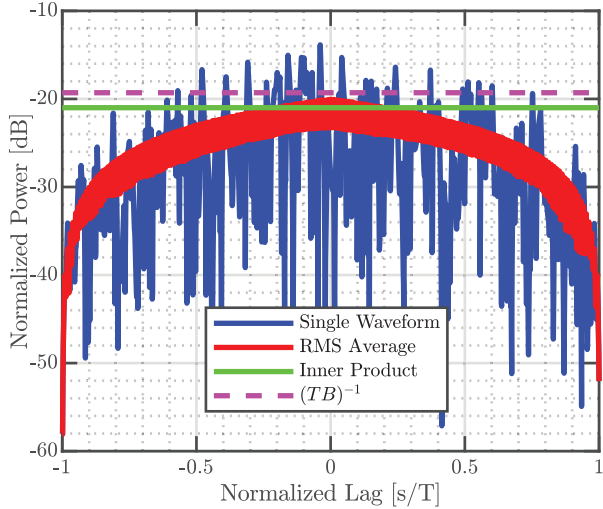


Fig. 7. Cross correlation for random phase codes ($TB = 85$) compared to predictions of expected correlation.

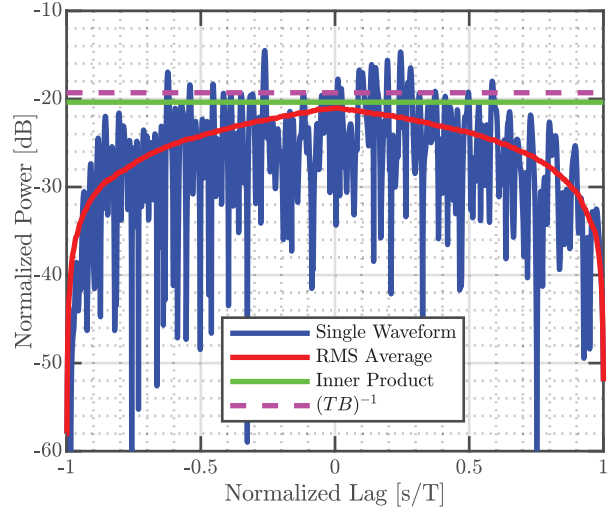


Fig. 9. Cross correlation for random super-Gaussian PRO-FM ($TB = 85$) compared to predictions of expected correlation.

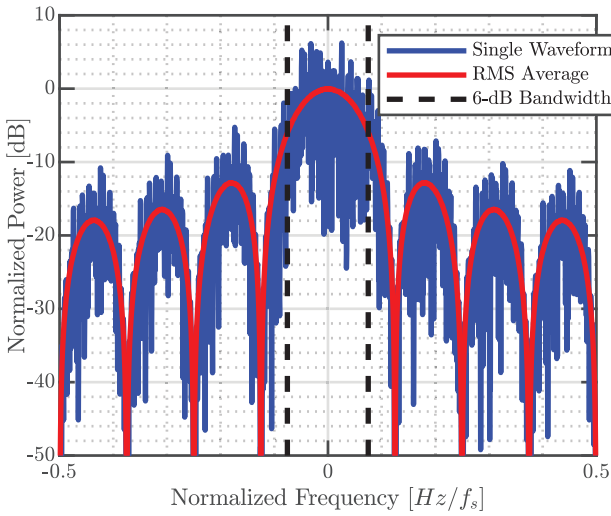


Fig. 8. PSD for random phase codes ($TB = 85$).

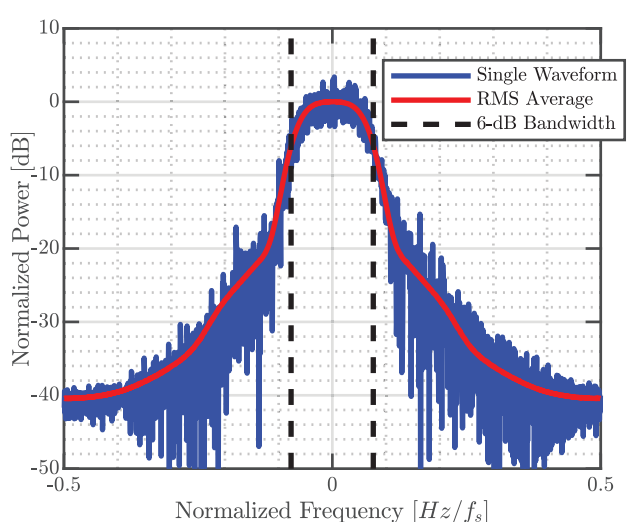


Fig. 10. PSD for random super-Gaussian PRO-FM ($TB = 85$).

given TB , the 6-dB rms bandwidth for phase codes is used to set the 6-dB bandwidth for the other waveform classes (for fair comparison). All waveforms were oversampled by 8 relative to their 6-dB bandwidths to ensure a high-fidelity representation.

Single-pair instantiations of cross correlation and PSD are also included, where we note that the highest sidelobe is generally not at zero lag. However, when the rms average is performed across the set of 10 000 trials, we do indeed find the zero lag to exhibit the highest value across all cases except the LFM benchmark. Rather different spectral shapes are also observed across the RFM waveform and random phase-code classes, though this distinction has no noticeable impact on cross correlation since all cases are restricted to 6-dB bandwidth.

B. High TB Case

Now, consider a relatively high per-pulse dimensionality of $TB = 1000$, which is consistent with imaging applications

TABLE II

ZERO-LAG EXPECTED CROSS CORRELATION VALUES ($TB = 1000$)

Waveform class	RMS average correlation (11)	Predicted correlation (9)
PCFM	-30.13 dB	-29.76 dB
CE-OFDM	-30.10 dB	-29.76 dB
PRO-FM	-30.04 dB	-29.61 dB
LFM up/down	-33.09 dB	-29.49 dB

like synthetic aperture radar (SAR). While phase codes were included above for illustration purposes, we henceforth omit them since they are known to experience greater transmitter distortion due to poor spectral containment [18]. Instead, for a fair comparison, the 6-dB design bandwidth is now set according to LFM swept bandwidth, which for $TB = 1000$ provides a separability of -30 dB via the inverse- TB heuristic.

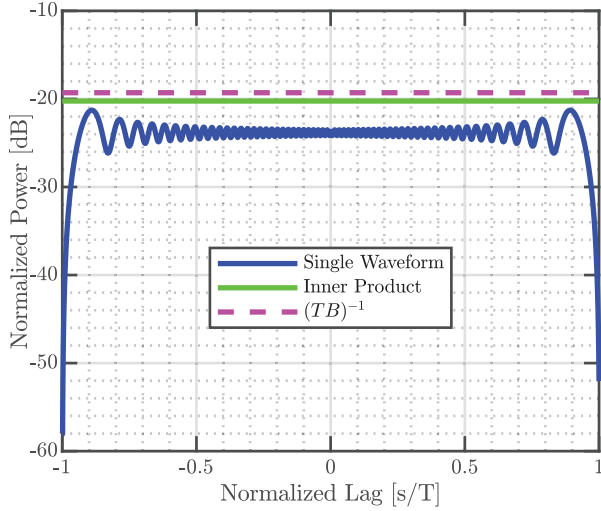


Fig. 11. Cross correlation for upchirp/downchirp LFM ($TB = 85$) compared to predictions of expected correlation.

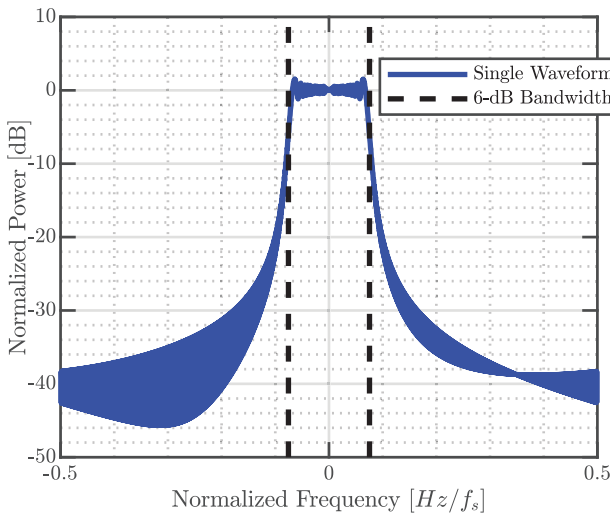


Fig. 12. PSD for LFM chirp ($TB = 85$).

Table II summarizes the simulated cross correlation values for this high TB case. For the RFM waveform classes, we again observe the level predicted by (9) that closely matches the empirical results using (11), now deviating by at most 0.4 dB. While the measured LFM upchirp/downchirp cross correlation is again about 3 dB better than the prediction (for the same reason as before), any differences between the various classes of random FM waveforms are now essentially negligible, suggesting that prediction via (9) improves as TB increases.

Figs. 13–20 illustrate the cross correlation and PSD plots for the different waveform classes. We see that rms-averaged responses (aside from LFM) have a peak at zero lag despite the randomness of where individual cross correlation peaks may occur. Indeed, the higher dimensionality now suggests greater roll-off to the general envelope of the single-instantiation cross correlations. This response in turn underscores why the mean peak would occur at zero lag.

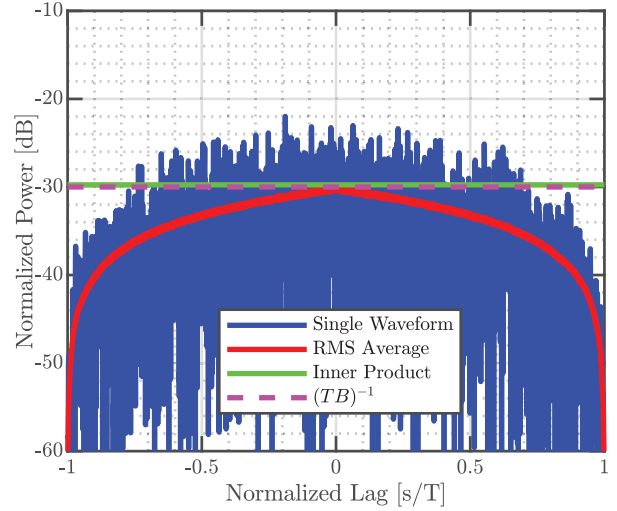


Fig. 13. Cross correlation for random 1st-order PCFM ($TB = 1000$) compared to predictions of expected correlation.

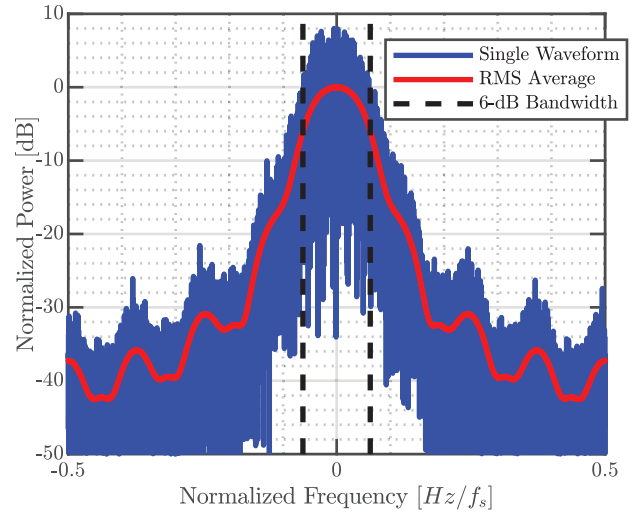


Fig. 14. PSD for random 1st-order PCFM ($TB = 1000$).

IV. EXPECTED MULTISTATIC INTERFERENCE FLOOR

Sections II–III have established the expected degree of cross correlation separability between arbitrary pairs of waveforms for a variety of different RFM classes. We now extend that analysis to assess the expected multistatic scattering interference one would encounter given a single point scatterer. For the sake of focusing on waveform separability, we explicitly consider a correlation-limited scenario and ignore noise, which in reality would simply be superimposed in the receiver.

A. Cross-Filtered Response

Consider that two unit-amplitude RFM waveforms defined as $s_1(t) = \exp(j\phi_1(t))$ and $s_2(t) = \exp(j\phi_2(t))$, for imaginary unit j , having common 6-dB bandwidth B (though the exact bandwidth definition is arbitrary), resulting in a Rayleigh range resolution proportional to $1/B$, and common pulsewidth T . For the sake of analysis, let the phase functions $\phi_1(t)$ and $\phi_2(t)$ be independent stationary random processes, uniformly distributed on $(-\pi, \pi)$. Note that this arrangement is an

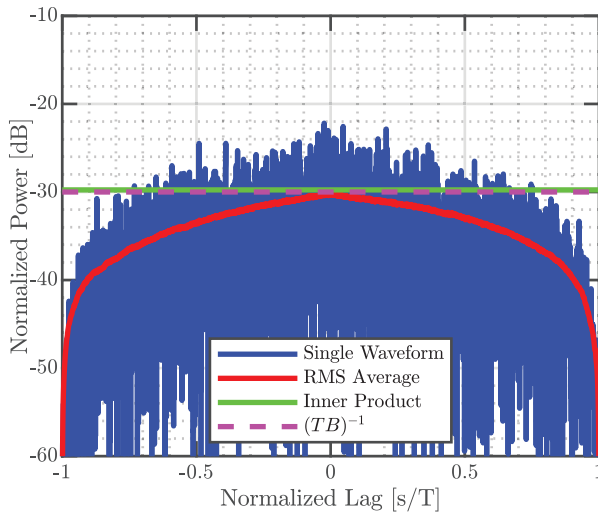


Fig. 15. Cross correlation for random CE-OFDM (TB = 1000) compared to predictions of expected correlation.

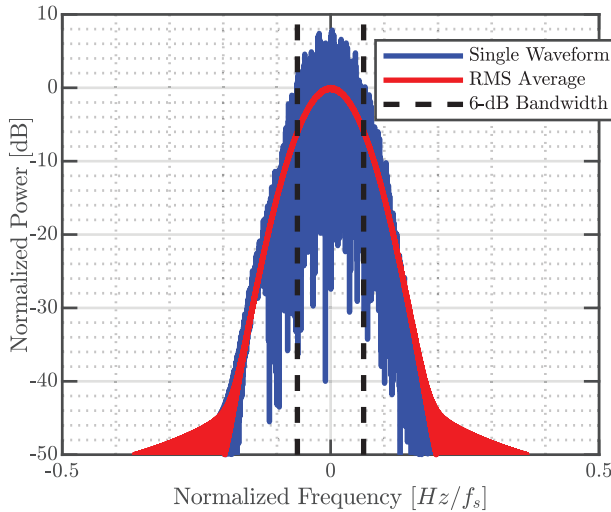


Fig. 16. PSD for random CE-OFDM (TB = 1000).

approximation for RFM waveforms, but it holds well for zero-symmetric phase distributions, which are descriptive of most practical RFM implementations. We also remind the reader that RFM waveforms possess a continuous-phase function, resulting in better spectral containment relative to phase codes. With spectral containment in mind, we wish to examine the statistical structure of the cross-filtered response, which is likewise a random process.

First, write the cross-filtered response as

$$c_{1,2}(\tau) = \int_{-T}^T s_1^*(t-\tau) s_2(t) dt. \quad (12)$$

To make use of the central limit theorem (CLT), apply the truncated sinc expansion (see Appendix D) to (12) so that

$$c_{1,2}(\tau) \approx \frac{1}{T} \int_{-\infty}^{\infty} \mathbf{p}^T(t-\tau) \mathbf{s}_1^* \mathbf{s}_2^T \mathbf{p}(t) dt \quad (13)$$

where $\mathbf{p}(t) = [p_0(t), p_1(t), \dots, p_{N-1}(t)]^T$ is the vector of sinc basis functions at time instant t , with $p_n(t) = \text{sinc}(t/T_s - n)$ for

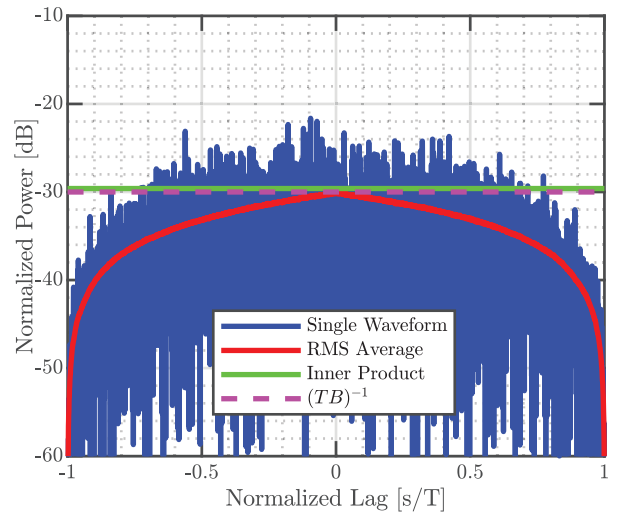


Fig. 17. Cross correlation for random super-Gaussian PRO-FM (TB = 1000) compared to predictions of expected correlation.

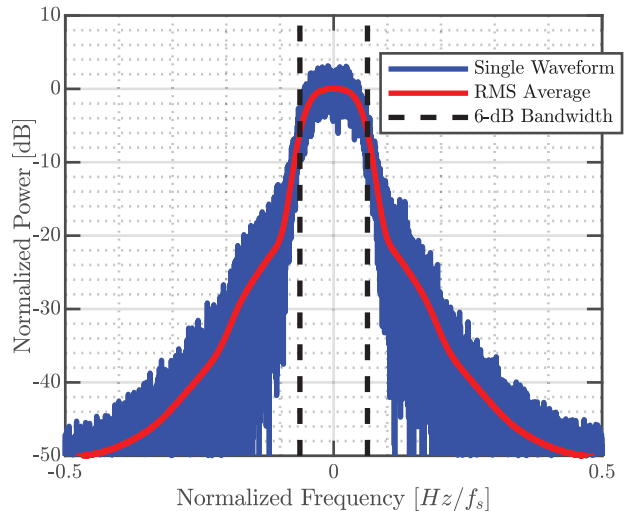


Fig. 18. PSD for random super-Gaussian PRO-FM (TB = 1000).

discrete integer sample index n and sampling interval $t_s = 1/B$. The critical sampling interval results in a random sequence of statistically independent waveform samples. Vectors \mathbf{s}_1 and \mathbf{s}_2 (here the sinc basis weights) are discretized representations of waveforms $s_1(t)$ and $s_2(t)$, respectively. Expanding the integral results in

$$\begin{aligned} & \int_{-\infty}^{\infty} \mathbf{p}^T(t-\tau) \mathbf{s}_1^* \mathbf{s}_2^T \mathbf{p}(t) dt \\ &= \int_{-\infty}^{\infty} \left\{ \sum_{m=0}^{N-1} s_{1,m}^* \text{sinc}\left(\frac{t-\tau}{\delta} - m\right) \times \left(\sum_{n=0}^{N-1} s_{2,n} \text{sinc}\left(\frac{t}{\delta} - n\right) \right) \right\} dt \\ &= \sum_{m=0}^{N-1} \sum_{n=0}^{N-1} s_{1,m}^* s_{2,n} \int_{-\infty}^{\infty} \left[\text{sinc}\left(\frac{t-\tau}{\delta} - m\right) \times \text{sinc}\left(\frac{t}{\delta} - n\right) \right] dt \end{aligned}$$

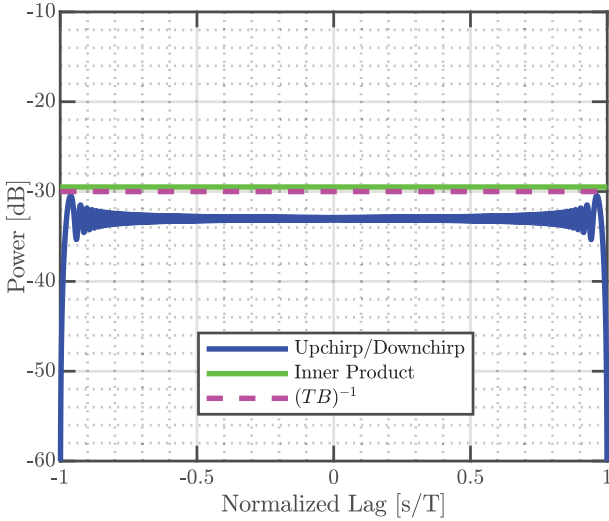


Fig. 19. Cross correlation for upchirp/downchirp LFM ($TB = 1000$) compared to predictions of expected correlation.

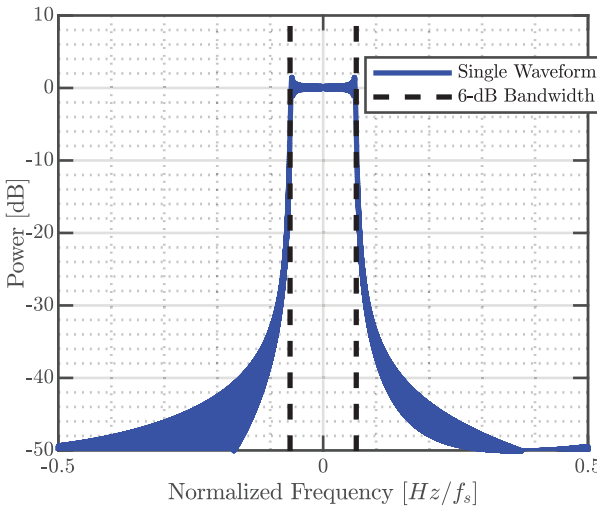


Fig. 20. PSD for LFM chirp ($TB = 1000$).

$$\begin{aligned}
 &= \sum_{m=0}^{N-1} \sum_{n=0}^{N-1} s_{1,m}^* s_{2,n} \text{sinc}\left((n-m) - \frac{\tau}{\delta}\right) \\
 &= \sum_{m=0}^{N-1} \sum_{n=0}^{N-1} s_{1,m}^* s_{2,n} P_{mn}(-\tau) \\
 &= \mathbf{s}_1^H \mathbf{P}(-\tau) \mathbf{s}_2
 \end{aligned} \tag{14}$$

which expresses the cross correlation as the generalized inner product between the waveform basis vectors evaluated at time τ via the sinc basis matrix $\mathbf{P}(-\tau)$.

Assuming that the waveforms are bandlimited (clearly an approximation for a time-limited pulse), we can space the basis functions in $\mathbf{P}(-\tau)$ by $\delta = 1/B$, which is equivalent to critical sampling. Under this assumption, the elements in vectors \mathbf{s}_1 and \mathbf{s}_2 are well-approximated as independent and identically distributed (IID).

Define the sinc-interpolated version of \mathbf{s}_2 as $\tilde{\mathbf{s}}_2(\tau) = \mathbf{P}(-\tau)\mathbf{s}_2$. Since we have assumed that the waveforms are bandlimited, the continuous-time signal $s_2(t)$ may be completely

reconstructed from the samples in \mathbf{s}_2 . Thus, the matrix $\mathbf{P}(-\tau)$ determines the interelement correlation of $\tilde{\mathbf{s}}_2(\tau)$ for any arbitrary delay τ . The mean of $\tilde{\mathbf{s}}_2(\tau)$ is the zero vector, as shown shortly in (16), while the covariance is $E\{\tilde{\mathbf{s}}_2(\tau)\tilde{\mathbf{s}}_2^H(\tau)\} = \mathbf{P}(-\tau)E\{\mathbf{s}_2\mathbf{s}_2^H\}\mathbf{P}^H(-\tau) \approx \mathbf{P}(-\tau)\mathbf{P}^H(-\tau)$, where the final approximation comes from the assumption that the waveforms are bandlimited and critically sampled (with IID samples) resulting in $E\{\mathbf{s}_2\mathbf{s}_2^H\} \approx \mathbf{I}_N$, where \mathbf{I}_N is the $N \times N$ identity matrix.

In the case where $\tau/\delta = i$, for i an integer, $\tilde{\mathbf{s}}_2(\tau)$ is an IID random vector, just like \mathbf{s}_2 . When $|i|$ is sufficiently smaller than T/δ , the inner product $\mathbf{s}_1^H \tilde{\mathbf{s}}_2(\tau)$ is asymptotically normally distributed by the CLT. When $|i|$ is near T/δ , corresponding to few overlapping samples in the inner product $\mathbf{s}_1^H \tilde{\mathbf{s}}_2(\tau)$, the underlying distribution is less predictable, though the low power for such lags suggests that these cases are insignificant compared to those with greater overlap between the waveforms. For the case where τ/δ is not an integer, $\tilde{\mathbf{s}}_2(\tau)$ can be viewed as a straddled interpolation of \mathbf{s}_2 , thereby introducing possible deviation from the CLT.

For worst case straddling, set $\tau/\delta = i/2$. In this case, simulation has confirmed that the samples of $\tilde{\mathbf{s}}_2(\tau)$ are approximately complex-normal random variables. A more rigorous proof can be made via the Lindeberg CLT [27], though empirical evidence was sufficient for our purpose. Thus, we can safely assume that the inner product $\mathbf{s}_1^H \tilde{\mathbf{s}}_2(\tau)$ is normally distributed by the CLT. By this argument, it can be inferred that $c_{1,2}(\tau)$ is normally distributed for all τ sufficiently away from the pulse edges $\pm T$.

Having established that the distribution of the cross-filtered response is asymptotically normal, we are able to characterize this process fully by computing its first and second moments. The mean is

$$\begin{aligned}
 E\{c_{1,2}(\tau)\} &= E\left\{\int_{-T}^T s_1^*(t-\tau) s_2(t) dt\right\} \\
 &= \int_{-T}^T E\{s_1^*(t-\tau)\} E\{s_2(t)\} dt
 \end{aligned} \tag{15}$$

where we have invoked the multiplicative separability of independent random processes under the expectation operator. The waveforms' expected values may be computed through use of the Law of The Unconscious Statistician (LOTUS) [29] via

$$\begin{aligned}
 E\{e^{j\phi(t)}\} &= \frac{1}{2\pi} \int_{-\pi}^{\pi} e^{j\phi(t)} d\phi(t) \\
 &= \frac{1}{2\pi} \int_{-\pi}^{\pi} [\cos(\phi(t)) + j \sin(\phi(t))] d\phi(t) \\
 &= \frac{1}{2\pi} [\sin(\phi(t)) - j \cos(\phi(t))]_{-\pi}^{\pi} \\
 &= 0
 \end{aligned} \tag{16}$$

showing that an RFM waveform with a uniformly distributed phase process (distributed on $[-\pi, +\pi]$) is zero mean. This result can be substituted into (15), yielding

$$E\{c_{1,2}(\tau)\} = 0. \tag{17}$$

Next, we compute the variance as

$$E\{|c_{1,2}(\tau)|^2\} = E\left\{\left|\frac{1}{\sqrt{E_1 E_2}} \int_{-T}^T s_1^*(t-\tau) s_2(t) dt\right|^2\right\}. \tag{18}$$

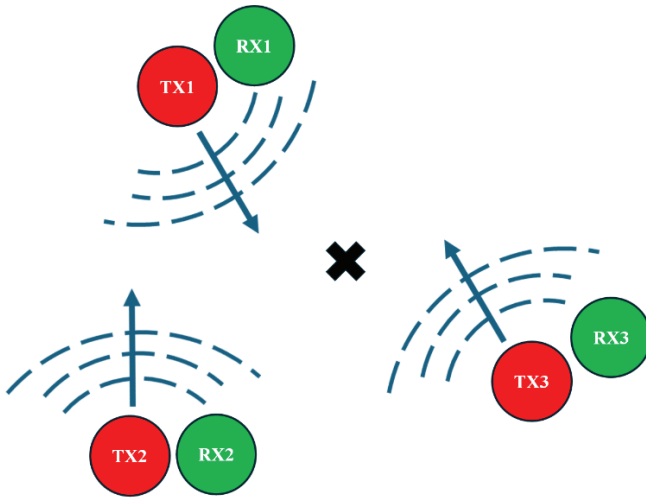


Fig. 21. Arbitrary multistatic geometry and a single point scatterer.

Per Section II, the variance of the cross-filtering process is equivalent to the mean square power of the cross correlation. Consequently, the variance can be approximated as

$$E \{ |c_{1,2}(\tau)|^2 \} \approx \frac{1}{TB} \quad (19)$$

which is derived in Appendix C.

B. Generalization to Multiple Emitters

Now, consider the effects of cross-filtered interference between an ensemble of K distributed, independently operating emitters, with each also possessing a collocated receiver. Each monostatic transmit/receive pair may have a completely distinct field of regard relative to the other $K - 1$ pairs and the spatial arrangement of the individual transmit/receive pairs is arbitrary. A single point scatterer is considered, with a graphical depiction illustrated in Fig. 21 for $K = 3$. For the convenience of ignoring extraneous delay terms, assume that the transmitters are synchronized and emit independent waveforms that are temporally and spectrally coincident, having the same time-bandwidth product. Consequently, the reflected signal captured at the k th receiver is the superposition of the K emitted waveforms reflected by the point scatterer, which when neglecting noise can be written simply as

$$y_k(t) = \sum_{l=0}^{K-1} \alpha_{k,l} s_l(t - \tau_{k,l}) \quad (20)$$

where $s_l(t)$ is the waveform emitted by the l th transmitter, $\tau_{k,l}$ is the propagation delay between the l th transmitter and the k th receiver, and $\alpha_{l,k}$ is the complex scattering for the l th and k th transmit/receive pair accounting for differing propagation loss and beam patterns. Note that the assumption of mutual synchronization between the transmitters allows the consideration of a single relative delay term $\tau_{k,l}$ per transmitter/receiver pair but does not affect the generality of the results. Applying

the matched filter to (20) according to the k th radar's transmit waveform then yields

$$\begin{aligned} r_k(\tau) &= \frac{1}{T} \int_{-T}^T s_k^*(t - \tau) \left(\sum_{l=0}^{K-1} \alpha_{k,l} s_l(t - \tau_{k,l}) \right) dt \\ &= \sum_{l=0}^{K-1} \alpha_{k,l} \frac{1}{T} \int_{-T}^T s_k^*(t - \tau) s_l(t - \tau_{k,l}) dt \\ &= \alpha_{k,k} c_{k,k}(\tau - \tau_{k,k}) + \sum_{\substack{l=0 \\ l \neq k}}^{K-1} \alpha_{k,l} c_{k,l}(\tau - \tau_{k,l}) \\ &= \alpha_{k,k} c_{k,k}(\tau - \tau_{k,k}) + z_k(\tau) \end{aligned} \quad (21)$$

where $c_{k,l}(\tau)$ is simply the generalization of (12) and $c_{k,k}(\tau)$ is therefore the autocorrelation function of the k th waveform. The final term $z_k(\tau)$ is comprised of the overall mutual interference induced by scattering from the other ($K - 1$) emitters.

To assess the impact of superimposed scattering from multiple emitters, we can repeat the previous mean/variance evaluation for $z_k(\tau)$ in (21). First, the mean is

$$\begin{aligned} E \{ z_k(\tau) \} &= E \left\{ \sum_{\substack{l=0 \\ l \neq k}}^{K-1} \alpha_{k,l} c_{k,l}(\tau - \tau_{k,l}) \right\} \\ &= \sum_{\substack{l=0 \\ l \neq k}}^{K-1} \alpha_{k,l} E \{ c_{k,l}(\tau - \tau_{k,l}) \} \\ &= 0 \end{aligned} \quad (22)$$

where the final result comes from (17), implying that the mean of the multistatic interference is zero regardless of the number of independent emitters. Likewise, the variance is

$$\begin{aligned} E \{ |z_k(\tau)|^2 \} &= E \left\{ \left| \sum_{\substack{l=0 \\ l \neq k}}^{K-1} \alpha_{k,l} c_{k,l}(\tau - \tau_l) \right|^2 \right\} \\ &= E \left\{ \left(\sum_{\substack{l=0 \\ l \neq k}}^{K-1} \alpha_{k,l} c_{k,l}(\tau - \tau_l) \right)^* \times \left(\sum_{\substack{m=0 \\ m \neq k}}^{K-1} \alpha_{k,m}^* c_{k,m}^*(\tau - \tau_m) \right) \right\} \\ &= \sum_{\substack{l=0 \\ l \neq k}}^{K-1} \sum_{\substack{m=0 \\ m \neq k}}^{K-1} \alpha_{k,l} \alpha_{k,m}^* E \left\{ c_{k,l}(\tau - \tau_l) \times c_{k,m}^*(\tau - \tau_m) \right\}. \end{aligned} \quad (23)$$

Due to the statistical independence of the waveforms, we can assert via Appendix C that

$$E \{ c_{k,l}(\tau - \tau_l) c_{k,m}^*(\tau - \tau_m) \} \approx \begin{cases} (TB)^{-1}, & m = l \\ 0, & \text{else.} \end{cases} \quad (24)$$

Substituting (24) into (23) therefore results in

$$E \{ |z_k(\tau)|^2 \} = \frac{1}{TB} \sum_{\substack{l=0 \\ l \neq k}}^{K-1} |\alpha_{k,l}|^2 \quad (25)$$

which provides the expected multistatic interference floor due to a single point scatterer when multiple emitters have perfectly overlapped spectra and operate concurrently.

A specific case of interest is a collocated multiple-input–multiple-output (MIMO) framework, where K emitters operate independently of essentially the same location (e.g., subarrays of a larger array) and have the same field of regard. Under this arrangement, we can normalize out the different scattering by setting $\alpha_{kl} = 1 \forall l \neq k$ so that (25) becomes

$$E\{|z_k(\tau)|^2\} = \frac{K-1}{TB} \quad (26)$$

which can be used as a general guideline for mutual interference of multiemitter systems.

C. Extension to Waveform-Agile Operation

Finally, since RFM waveforms are intended for use in a nonrepeating manner to realize their high-dimensional benefits, we further extend the above analysis to now account for waveform agility as well. Start by letting each of the K radars emit a sequence of Q independent RFM waveforms, again assuming that the transmitters are synchronized (for convenience of analysis) and have the same time–bandwidth product. We likewise again assume a simple point scatterer and neglect noise.

We can therefore extend (20) as

$$y_{k,p}(t) = \sum_{l=0}^{K-1} \alpha_{k,l,p} s_{l,p}(t - \tau_{k,l}) \quad (27)$$

for $q = 1, 2, \dots, Q$, where $s_{l,q}(t)$ is the q th pulsed waveform emitted by the l th transmitter and the scattering $\alpha_{k,l,q}$ is made dependent on q to account for Doppler. Like (21), applying the matched filter to the q th pulse response for the k th radar yields

$$\begin{aligned} r_{k,q}(\tau) &= \frac{1}{T} \int_{-T}^T s_{k,q}^*(t - \tau) \left(\sum_{l=0}^{K-1} \alpha_{k,l,q} s_{l,q}(t - \tau_{k,l}) \right) dt \\ &= \sum_{l=0}^{K-1} \alpha_{k,l,q} \frac{1}{T} \int_{-T}^T s_{l,q}^*(t - \tau) s_{l,q}(t - \tau_{k,l}) dt \\ &= \alpha_{k,k,q} c_{k,k,q}(\tau - \tau_{k,k}) + \sum_{\substack{l=0 \\ l \neq k}}^{K-1} \alpha_{k,l,q} c_{k,l,q}(\tau - \tau_{k,l}) \\ &= \alpha_{k,k,q} c_{k,k,q}(\tau - \tau_{k,k}) + z_{k,q}(\tau) \end{aligned} \quad (28)$$

where we have also neglected range walking so that all the $\tau_{k,l}$ terms remain constant across slow time (for simplicity). Once again, the final term $z_{k,q}(\tau)$ is comprised of the mutual interference induced by scattering from the other ($K-1$) emitters, albeit now across the coherent processing interval (CPI) of Q pulses.

The next processing stage would generally involve a Fourier transform across slow time to provide discrimination in Doppler/cross-range. Doing so also realizes a coherent gain on the $\alpha_{k,k,q} c_{k,k,q}(\tau - \tau_{k,k})$ term in (28) relative to components that are not coherent across slow time (e.g., mutual interference). Let the normalized discrete Fourier transform matrix be

denoted as $(1/Q) \mathbf{D}$, which when applied would produce the vector

$$\tilde{z}_k(\tau) = \frac{1}{Q} \mathbf{D} [z_{k,0}(\tau) \ z_{k,1}(\tau) \ \cdots \ z_{k,Q-1}(\tau)]^T \quad (29)$$

for the mutual interference relative to the k th radar. Since this term is not coherent, we can examine the n th element of (29) for any arbitrary Doppler frequency via application of \mathbf{d}_n (the n th row vector of \mathbf{D}). This response can be expressed as

$$\begin{aligned} \tilde{z}_{k,n}(\tau) &= \frac{1}{Q} \mathbf{d}_n [z_{k,0}(\tau) \ z_{k,1}(\tau) \ \cdots \ z_{k,Q-1}(\tau)]^T \\ &= \frac{1}{Q} \sum_{p=0}^{Q-1} d_{n,q} \sum_{\substack{l=0 \\ l \neq k}}^{K-1} \alpha_{k,l,q} c_{k,l,q}(\tau - \tau_{k,l}) \\ &= \frac{1}{Q} \sum_{q=0}^{Q-1} \sum_{\substack{l=0 \\ l \neq k}}^{K-1} \tilde{\alpha}_{k,l,q} c_{k,l,q}(\tau - \tau_{k,l}) \end{aligned} \quad (30)$$

where we have simply subsumed the (here arbitrary) Fourier coefficient into the scattering term as $\tilde{\alpha}_{k,l,q} = d_{n,q} \alpha_{k,l,q}$.

It follows from (22) that taking the expectation of (30) likewise realizes a mean of zero. The variance, which established the expected power level of the interference floor, is computed as

$$\begin{aligned} E\{|\tilde{z}_{k,n}(\tau)|^2\} &= E\left\{ \left| \frac{1}{Q} \sum_{q=0}^{Q-1} \sum_{\substack{l=0 \\ l \neq k}}^{K-1} \tilde{\alpha}_{k,l,q} c_{k,l,q}(\tau) \right|^2 \right\} \\ &= \frac{1}{Q^2} E\left\{ \left(\sum_{q_1=0}^{Q-1} \sum_{\substack{l_1=0 \\ l_1 \neq k}}^{K-1} \tilde{\alpha}_{k,l_1,q_1} c_{k,l_1,q_1}(\tau) \right) \right. \\ &\quad \times \left. \left(\sum_{q_2=0}^{Q-1} \sum_{\substack{l_2=0 \\ l_2 \neq k}}^{K-1} \tilde{\alpha}_{k,l_2,q_2} c_{k,l_2,q_2}(\tau) \right)^* \right\} \\ &= \frac{1}{Q^2} \sum_{q_1=0}^{Q-1} \sum_{\substack{l_1=0 \\ l_1 \neq k}}^{K-1} \sum_{q_2=0}^{Q-1} \sum_{\substack{l_2=0 \\ l_2 \neq k}}^{K-1} \\ &\quad \times \left[\tilde{\alpha}_{k,l_1,q_1} \tilde{\alpha}_{k,l_2,q_2} \times E\{c_{k,l_1,q_1}(\tau) c_{k,l_2,q_2}^*(\tau)\} \right]. \end{aligned} \quad (31)$$

Because of the independence of waveforms across emitters, the variance can be simplified via (24) since a nonzero result is obtained only when $l_1 = l_2$ and $q_1 = q_2$, thereby yielding

$$E\{|\tilde{z}_{k,n}(\tau)|^2\} = \frac{1}{QTB} \sum_{\substack{l=0 \\ l \neq k}}^{K-1} |\alpha_{k,l}|^2 \quad (32)$$

with l_1 and l_2 now replaced with l for simplicity. Here, we have assumed that the scatterer only changes phase over the CPI for each transmitter/receiver pair.

The collocated MIMO framework in Section IV-B set $\alpha_{lk} = 1 \forall l \neq k$, subsequently producing the separability guideline in (26). Doing likewise for (32) realizes

$$E\{|\tilde{z}_{k,n}(\tau)|^2\} = \frac{K-1}{QTB} \quad (33)$$

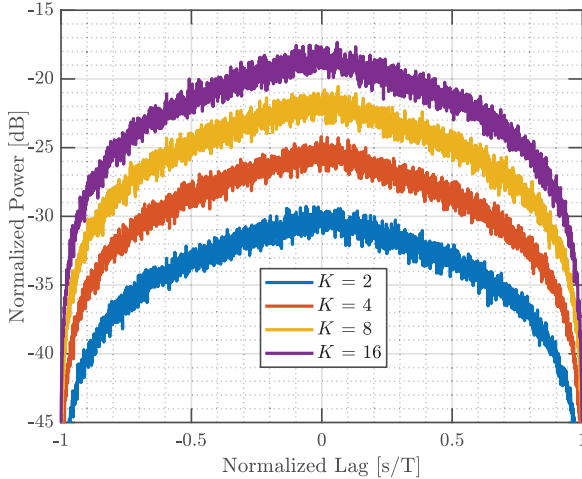


Fig. 22. Expected rms cross correlation for $Q = 1$ RFM waveform for each of K different emitters, which agrees with (31).

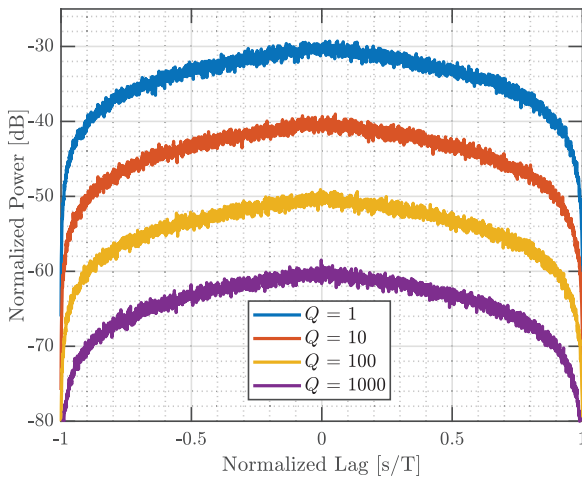


Fig. 23. Expected rms cross correlation for $K = 2$ RFM emitters after Doppler processing across Q independent waveforms, which agrees with (38).

which in turn provides a general guideline for the mutual interference in each Doppler bin for K independent emitters using waveform agility.

A simulated Monte Carlo example for this hypothesized multistatic/waveform-agile arrangement is shown in Figs. 22 and 23. Here, rms cross correlation responses are generated for different numbers of emitters K and pulses Q when using 100 waveforms having $\text{TB} = 1000$. These numerical results clearly depict agreement with (26) and (33).

V. EXPECTED MAXIMUM CORRELATION

Having now examined the expected power for the zero-lag sample of the cross correlation of two RFM waveforms possessing similar spectral and temporal support, we turn our attention to the worst case correlation. At first glance, it would seem that the peak correlation value should occur at zero lag, due to this value possessing the highest possible variance (a function of waveform overlap). Despite this, the stochastic nature of RFM waveforms suggests that the maximum correlation value can occur for any time lag. We therefore seek

to justify the examination of the correlation function at zero lag.

Similar to previous analyses, consider the normalized cross correlation $c_{1,2}(\tau)$ between two independent RFM waveforms $s_1(t)$ and $s_2(t)$. Then, define the maximum correlation as

$$M = \max_{\tau} \{ |c_{1,2}(\tau)| \}. \quad (34)$$

Note that the cross correlation function will be weighted by a triangular window corresponding to the convolution between the rectangular pulse shapes of $s_1(t)$ and $s_2(t)$ (assuming FM waveforms), meaning that we can safely assume that the maximum correlation will most likely occur at $\tau = 0$ on average (assuming that the correlating signals have equal time support). Given that $c_{1,2}(0)$ is a random variable, we can approximate M as the maximum value across an ensemble of K realizations of the correlation function, evaluated at zero lag, or

$$M \approx \max \{ |c_1(0)|, |c_2(0)|, \dots, |c_K(0)| \} \quad (35)$$

where $c_k(0)$ is the k th correlation function at zero lag. Thus, the estimation of M requires derivation of its pdf as $K \rightarrow \infty$, which can be seen as an extension of the central limit theory. The maximum value of random variables is the *last order statistic*, the study of which is described by the extreme value theory (EVT) [29]. To apply the techniques of EVT, write the k th correlation function as

$$c_k(0) = \int_{-\infty}^{\infty} s_{1,k}^*(t-0) s_{2,k}(t) dt \quad (36)$$

where $s_{1,k}(t)$ and $s_{2,k}(t)$ are the k th realizations of waveform 1 and 2, respectively, which contribute to the K correlation functions over which M is estimated in (35). As shown in Section IV-A, $c_k(\tau)$ is a Gaussian random process, which we will approximate as memoryless and stationary. Treating the set $|c_1(0)|, |c_2(0)|, \dots, |c_K(0)|$ as IID Gaussian random variables, a claim established and verified in Section IV-A. We can assert that the distribution of $|c_k(\tau)|$ is Rayleigh.

The maximum value of a set of IID random variables is statistically described by the extreme value distribution, which contains a family of well-known distributions such as Gumbel, Frechet, and Weibull. Of particular interest is the Gumbel distribution that describes the maximum of random variables whose individual PDFs are of the form [29]

$$P(X = x) = af'(x)e^{f(x)} \quad (37)$$

where $f(x)$ is an arbitrary continuous transformation on random variable X , $f'(x)$ is the derivative of $f(x)$ with respect to x , and a is a scalar set to ensure that $P(X)$ integrates to unity. Included among this class of distributions is the Rayleigh distribution. Thus, let $f(x) = -(x^2/2\sigma^2)$ for parameter σ^2 and $a = -1$. Then, the Rayleigh distribution is written as

$$P(X = x) = \frac{x}{\sigma^2} e^{-\frac{x^2}{2\sigma^2}}. \quad (38)$$

Given the form of the Rayleigh distribution and since M is defined as the maximum over a set of Rayleigh random

variables, we can assert that M is characterized by the Gumbel distribution. For an extreme-valued random variable, the Gumbel distribution is given as

$$P(X = x) = \frac{1}{\beta} e^{-\frac{x-\mu}{\beta}} e^{-e^{-\frac{x-\mu}{\beta}}} \quad (39)$$

for real scale parameter β and real location parameter μ . We wish to estimate β and μ by maximizing the likelihood function. Consider a K -length IID snapshot vector of realizations of extreme value index X , that is, $\mathbf{X} = \mathbf{x} = [x_0, x_1, \dots, x_{K-1}]^T$. The likelihood function for this random vector $P(\mathbf{X} = \mathbf{x})$ is given by

$$P(\mathbf{X} = \mathbf{x}) = \prod_{k=0}^{K-1} \frac{1}{\beta} e^{-\frac{x_k-\mu}{\beta}} e^{-e^{-\frac{x_k-\mu}{\beta}}}. \quad (40)$$

Maximization of (40) with respect to μ and β results in a system of nonlinear equations that must be solved numerically, as described in [30]. To realize a closed-form solution to the maximization of (40) that is purely dependent on waveform parameters, we can consider a second-order Taylor expansion of the likelihood function, which is posed and solved in Appendix E. An appropriate point for the Taylor expansion is found via a log-domain regression on Monte Carlo data. From these procedures, maximum-likelihood estimates for the scale and location parameters, denoted as $\hat{\mu}_{ML}$ and $\hat{\beta}_{ML}$, respectively, are found to be

$$\hat{\mu}_{ML} \approx \mu_0 + \frac{-a_0(b_1 + 2b_0^2) + b_0(a_2 + 2a_0b_0)}{(a_1 + 2a_0^2)(b_1 + 2b_0^2) - (a_2 + 2a_0b_0)^2} \quad (41)$$

and

$$\hat{\beta}_{ML} \approx \beta_0 + \frac{-b_0(a_1 + 2a_0^2) + a_0(a_2 + 2a_0b_0)}{(a_1 + 2a_0^2)(b_1 + 2b_0^2) - (a_2 + 2a_0b_0)^2} \quad (42)$$

where the constants a_0, a_1, a_2, b_0 , and b_1 are given in Appendix E by (E.11a)–(E.11e), and the expansion points μ_0 and β_0 are

$$\mu_0 = 10^{\frac{-c_1 \log(TB) + c_2}{20}} - \gamma \beta_0 \quad (43)$$

and

$$\beta_0 = \left(\frac{\pi^2}{6} 10^{\frac{-c_3 \log(TB) + c_4}{10}} \right)^{\frac{1}{2}} \quad (44)$$

with the corresponding constants c_1 – c_4 solved for via least squares regression in Appendix E.

The utility of (41) and (42) becomes apparent when one considers that no data need to be generated to obtain these estimates. Consequently, the maximum correlation value can be predicted for a given time-bandwidth product via the expected value and variance of a Gumbel random variable, which are given by

$$E\{M\} \approx \hat{\mu}_{ML} + \gamma \hat{\beta}_{ML} \quad (45)$$

and

$$\text{Var}\{M\} \approx \frac{\pi^2}{6} \hat{\beta}_{ML}^2. \quad (46)$$

Using (41)–(44), we can determine a confidence interval for the approximate maximum-likelihood estimates for the maximum cross correlation value. Using numerical integration

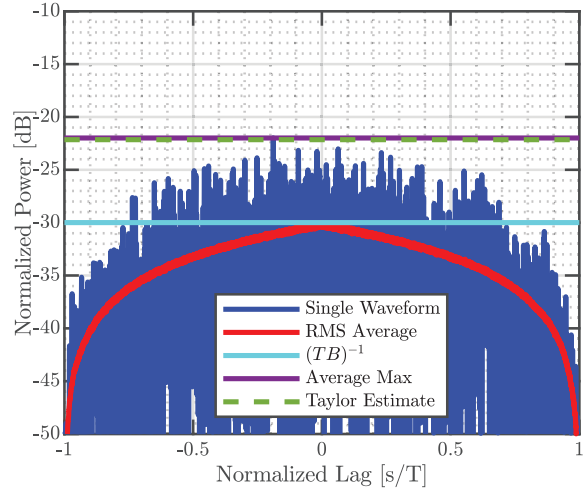


Fig. 24. Random 1st-order PCFM cross correlation ($TB = 1000$) compared to metrics for worst case correlation.

TABLE III
ENSEMBLE-AVERAGED MAXIMUM CORRELATION

Waveform	Average Max
PCFM	-22.08 dB
CE-OFDM	-21.97 dB
PRO-FM	-21.86 dB
LFM	-30.46 dB

(i.e., a Riemann sum), the 95% confidence interval for the maximum correlation value is

$$M \in \hat{\mu}_{ML} + (\gamma \hat{\beta}_{ML} - 2.98 \hat{\beta}_{ML}, \gamma \hat{\beta}_{ML} + 2.98 \hat{\beta}_{ML}). \quad (47)$$

This interval indicates, with 95% certainty, that the true value of the maximum cross correlation will lie within 2.32 standard deviations of the approximate maximum-likelihood estimate defined by (45).

VI. SIMULATION FOR MAXIMUM CROSS CORRELATION

To assess the derived estimates for the maximum cross correlation, consider a per-pulse dimensionality of $TB = 1000$. It should be noted that the following analysis has also been conducted for the $TB = 85$ case discussed in Section III, but the results are omitted because they were not meaningfully different than for $TB = 1000$ below, apart from the ~ 10.7 -dB increase in the overall correlation level. Similar to Section III, 10 000 cross correlation responses are generated from the same 20 000 independent waveforms used for the results in Section III-B. These responses are compared with the maximum-likelihood estimate derived from the Taylor expansion [see (41) and (42)], which is here computed to be -22.154 dB as well as the average maximum magnitude observed over the ensemble of responses. The results of these comparisons are shown in Figs. 24–27. Table III also lists the observed ensemble-averaged, maximum correlation values, compared with the Taylor expansion-derived estimate.

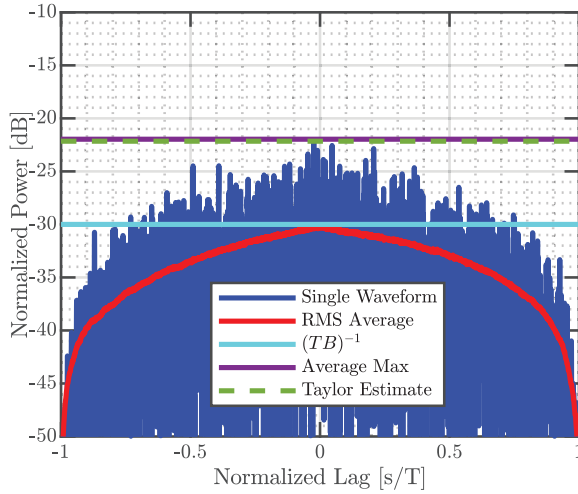


Fig. 25. Random CE-OFDM cross correlation ($\text{TB} = 1000$) compared to metrics for worst case correlation.

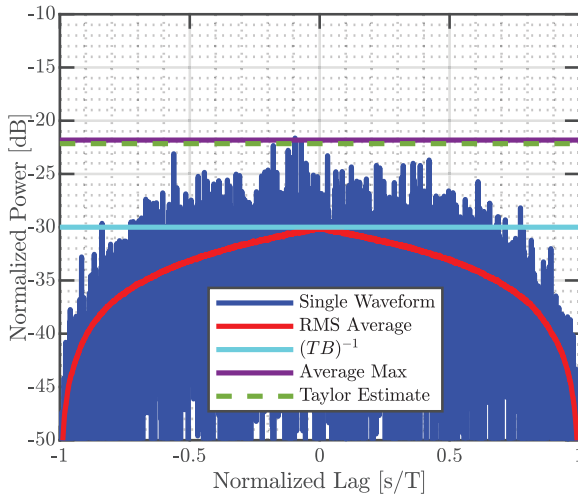


Fig. 26. PRO-FM cross correlation ($\text{TB} = 1000$) compared to metrics for worst case correlation.

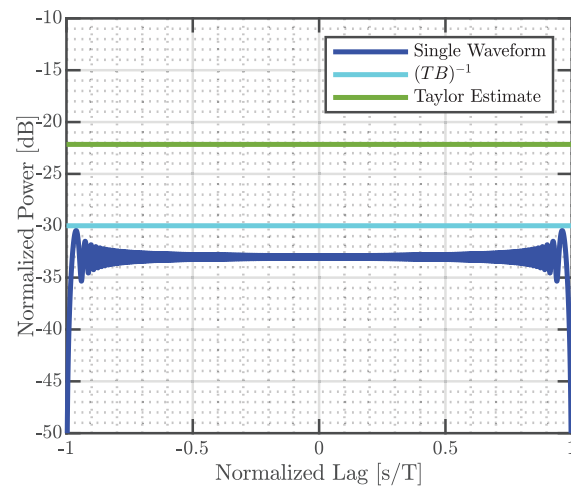


Fig. 27. LFM upchirp-downchirp cross correlation ($\text{TB} = 1000$) compared to metrics for worst case correlation.

For RFM waveforms, we see that the ensemble-averaged maximum values listed in Table III are all within a half decibel

of the Taylor-expanded estimates, suggesting that although the Taylor-expanded solution provides an approximately statistically optimal estimate for maximum cross correlation, the regression model given by (43) should generally provide an adequate substitution. We also note that LFM, being an entirely deterministic waveform, does not experience outliers in the way that the RFM waveforms do. Consequently, the LFM cross correlation peak is more than 8 dB lower than the maxima observed for random waveforms.

VII. CONCLUSION

It has long been observed that the separability between radar waveforms is dependent on the inverse of the time–bandwidth product shared between the interfering signals, herein termed the *mutual time–bandwidth product*. Here, we have established both statistical and analytical frameworks through which the average separability between interfering RFM waveforms can be assessed. The analytically derived predictor for waveform separability is found to compare well to the inverse-TB heuristic. Furthermore, the cross correlation can be predicted, based on the mutual time–bandwidth product, and accounted for in system design, which could enable maximal spectral utilization for multistatic radars.

Since randomly generated radar waveforms exhibit stochastically varying cross correlations, the analytically derived average correlation is insufficient for predicting the maximum correlation value. A hybrid approach, leveraging both EVT and high-dimensional Monte Carlo simulations, is used to provide a closed-form predictor of the maximum cross correlation and verify the resultant expressions. In this way, robust predictors for average and maximum expected cross correlation values are derived that are based solely on waveform parameters, meaning that no data generation is required.

APPENDIX A DERIVATION OF THE MULTI-LFM CROSS CORRELATION

It is noted herein that the cross correlation of an upchirp/downchirp waveform pair produces an idealized response, with a zero-lag power roughly 3 dB lower than interfering RFMs of similar dimensionality. However, the ripple near the edges of the cross correlation produces values very near the $1/\text{TB}$ heuristic for arbitrary interfering waveforms. Here, the analytical cross correlation between interfering chirp waveforms is derived, which provides an analytical baseline against which the statistical derivations from other sections are compared. Though a restricted version of this derivation has been considered before [31], it is here considered more generally.

First, let the i th interfering chirp waveform be expressed as

$$s_i(t) = a_i \exp\left(j2\pi\left(\frac{c_i}{2}t^2 + f_i t\right)\right), \quad t \in (0, T_i) \quad (\text{A.1})$$

where a_i is the pulse amplitude for $i \in \{1, 2\}$, T_i is the pulsedwidth, $c_i = B_i/T_i$ is chirp rate for waveform i and bandwidth B_i , and f_i is the i th start frequency. Without loss of

generality, assume that $T_1 \leq T_2$. From (1), the cross correlation between two interfering chirp waveforms is

$$\begin{aligned} & \sqrt{E_1 E_2} c_{1,2}(\tau) \\ &= \int_{-\infty}^{\infty} \left\{ \exp \left(-j2\pi \left(\frac{c_1}{2}(t-\tau)^2 + f_1(t-\tau) \right) \right) \right\} dt \quad (\text{A.2}) \end{aligned}$$

for waveform energies $E_i = a_i^2/T_i$.

By combining the quadratic phase arguments in (A.2), the cross correlation is rewritten as

$$c_{1,2}(\tau) = \frac{1}{\sqrt{E_1 E_2}} \int_{-\infty}^{\infty} \exp \left(j\frac{\pi}{2} (a(\tau)t^2 + b(\tau)t + c(\tau)) \right) dt \quad (\text{A.3})$$

where

$$\begin{aligned} a(\tau) &= 2(c_2 - c_1) \\ b(\tau) &= 4(c_1\tau + f_2 - f_1) \\ c(\tau) &= 4 \left(f_1\tau - \frac{1}{2}c_1\tau^2 \right). \end{aligned} \quad (\text{A.4})$$

By completing the square for the quadratic phase argument in (A.3), the cross correlation is simplified to

$$c_{1,2}(\tau) = \frac{e^{j\frac{\pi}{2} \left(c(\tau) - \frac{b^2(\tau)}{4a(\tau)} \right)}}{\sqrt{E_1 E_2}} \int_{-\infty}^{\infty} \exp \left(j\frac{\pi}{2} a(\tau) \left(t + \frac{b(\tau)}{2a(\tau)} \right)^2 \right) dt. \quad (\text{A.5})$$

To further simplify the cross correlation, we perform a change of integration variables to $g(t; \tau) = \sqrt{a(\tau)}(t + (b(\tau)/2a(\tau)))$. This results in

$$c_{1,2}(\tau) = \kappa(\tau) \int_{-\infty}^{\infty} \exp \left(j\frac{\pi}{2} g^2(t; \tau) \right) dg \quad (\text{A.6})$$

where

$$\kappa(\tau) = \frac{\exp \left(j\frac{\pi}{2} \left(c(\tau) - \frac{b^2(\tau)}{4a(\tau)} \right) \right)}{\sqrt{E_1 E_2 a(\tau)}}. \quad (\text{A.7})$$

The integral in (A.6) is computed, according to the limits of integration determined by the pulsedwidths of the two interfering waveforms, yielding

$$\begin{aligned} \int_{-\infty}^{\infty} \exp \left(j\frac{\pi}{2} g^2(t; \tau) \right) dg &= \int_{g(0)}^{g(\tau+T_1)} \exp \left(j\frac{\pi}{2} g^2(t; \tau) \right) dg \\ &+ \int_{g(\tau)}^{g(\tau+T_1)} \exp \left(j\frac{\pi}{2} g^2(t; \tau) \right) dg \\ &+ \int_{g(\tau)}^{g(T_2)} \exp \left(j\frac{\pi}{2} g^2(t; \tau) \right) dg \end{aligned} \quad (\text{A.8})$$

where the parameterization on τ has been dropped from the limits of integration for simplicity. Through application of the fundamental theorem of calculus, (A.8) may be rewritten in terms of the complex normalized Fresnel integral, which is defined as

$$F(\tau) = \int_0^{\tau} \exp \left(j\frac{\pi}{2} t^2 \right) dt \quad (\text{A.9})$$

thereby resulting in

$$\begin{aligned} c_{1,2}(\tau) &= \kappa(\tau) \begin{cases} F(g(\tau+T_1)) - F(g(0)) & \tau \in (-T_1, 0) \\ F(g(\tau+T_1)) - F(g(\tau)) & \tau \in (0, T_2 - T_1) \\ F(g(T_2)) - F(g(\tau)) & \tau \in (T_2 - T_1, T_2) \end{cases} \end{aligned} \quad (\text{A.10})$$

for

$$g(t; \tau) = \sqrt{2(c_2 - c_1)} \left(t + \frac{c_1\tau + f_2 - f_1}{c_2 - c_1} \right). \quad (\text{A.11})$$

Since much of this article involves analysis of waveforms that are perfectly coincident in time and frequency, we now simplify (A.10) for this scenario. Consider the case of two interfering baseband chirps with identical bandwidths and pulsedwidths, but opposite start frequencies and chirp rates. Consequently, the middle portion of (A.10) vanishes and the zero-lag power of the cross correlation becomes

$$\begin{aligned} |c_{1,2}(0)|^2 &= \frac{T}{4E_1 E_2 B} |F(g(T)) - F(g(0))|^2 \\ &= \frac{1}{a_1^2 a_2^2 \text{TB}} |F(\sqrt{\text{TB}})|^2 \end{aligned} \quad (\text{A.12})$$

which indicates the inverse-TB dependency of the upchirp/downchirp cross correlation. This result can be further simplified by letting $a_1 = a_2 = 1$, and noting that for $\text{TB} \geq 10$, the term $F(\sqrt{\text{TB}}) \approx 1/2$, which yields

$$|c_{1,2}(0)|^2 \approx \frac{0.5}{\text{TB}}. \quad (\text{A.13})$$

The approximation in (A.13) further emphasizes the 3-dB difference in zero-sample correlation observed between the LFM and RFM waveforms observed in Section I.

Furthermore, the ripple at the edges of the upchirp/downchirp cross correlation indicates that the maximum LFM upchirp/downchirp cross correlation is approximately

$$M \approx \frac{0.9}{\text{TB}}. \quad (\text{A.14})$$

Thus, when the ripple is accounted for, the upchirp/downchirp waveform pair provides nearly the same peak cross correlation as random waveforms having the same TB.

The analytical expression in (A.10) was compared to the numerical cross correlation for two chirp waveforms, implemented according to (1). The results are depicted in Figs. 28 and 29, with the corresponding waveform parameters for each test listed in Table IV. In Fig. 28, an upchirp and downchirp with identical pulsedwidths and bandwidths are cross correlated at baseband. Note that the analytical and numerical traces exactly coincide (within negligible errors due to sampling the waveforms for numerical implementation).

As a second demonstration of the efficacy of (A.10), two chirp waveforms were generated with differing pulsedwidths, bandwidths, and center frequencies, as indicated in Table IV. The resulting correlation functions are shown in Fig. 29, where the analytical result again overlays the numerical assessment exactly.

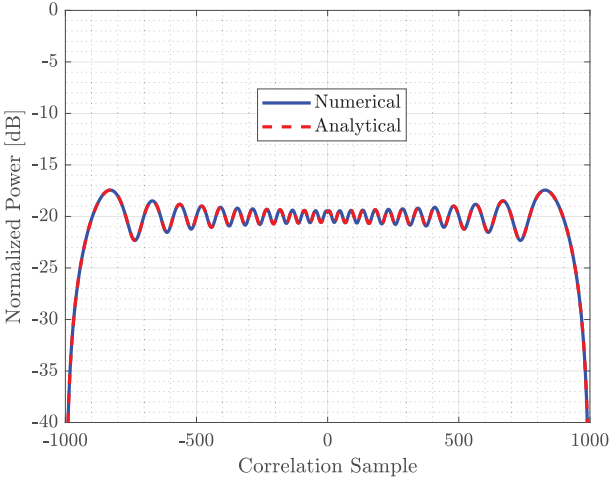


Fig. 28. Comparison of numerically and analytically implemented cross correlations between LFM waveforms with opposite chirp rates.

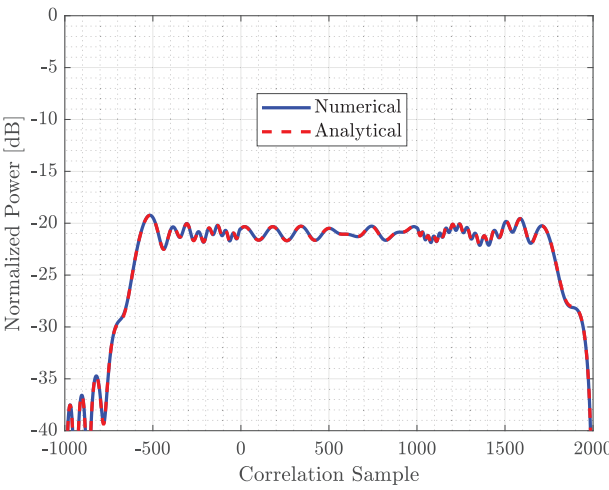


Fig. 29. Comparison of numerically and analytically implemented cross correlations between LFM waveforms with differing pulsewidths, bandwidths, and start frequencies.

TABLE IV
CHIRP CROSS CORRELATION PARAMETERS

	Fig. 28	Fig. 29
T_1	1 μ s	0.5 μ s
T_2	1 μ s	1 μ s
B_1	50 MHz	100 MHz
B_2	50 MHz	50 MHz
c_1	50 MHz/ μ s	50 MHz/ μ s
c_2	-50 MHz/ μ s	-50 MHz/ μ s
f_1	0 Hz	10 MHz
f_2	0 Hz	0 Hz

APPENDIX B PROOF THAT THE INNER PRODUCT CORRELATION ESTIMATE IS PURELY REAL

To confirm that the inner product method for computing the expected power of the zero-lag cross correlation provides

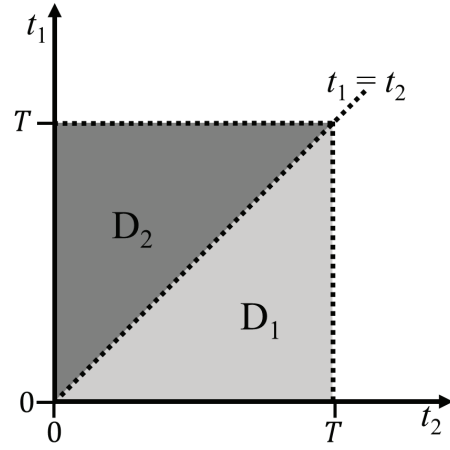


Fig. 30. Integration regions for cross correlation of pulsed signals.

a purely real result, use the conjugate symmetry property of the autocorrelation, i.e.,

$$R_{ii}(t_1, t_2) = R_{ii}^*(t_2, t_1). \quad (\text{B.1})$$

Applying (B.1) to the product of autocorrelations in (7) results in

$$R_{11}^*(t_1, t_2) R_{22}(t_1, t_2) = R_{11}(t_2, t_1) R_{22}^*(t_2, t_1) \quad (\text{B.2})$$

meaning that the product of the two autocorrelations is conjugate symmetric about the line $t_1 = t_2$. Consequently, we can rewrite the 2-D inner product from (7) as the integral sum

$$\begin{aligned} & \langle R_{22}(t_1, t_2), R_{11}(t_1, t_2) \rangle_{t_1, t_2} \\ &= \int_0^T \int_0^T R_{11}^*(t_1, t_2) R_{22}(t_1, t_2) dt_1 dt_2 \\ &= \iint_{D_1} R_{11}^*(t_1, t_2) R_{22}(t_1, t_2) dt_1 dt_2 \\ &\quad + \iint_{D_2} R_{11}^*(t_1, t_2) R_{22}(t_1, t_2) dt_1 dt_2 \\ &= \iint_{D_1} R_{11}^*(t_1, t_2) R_{22}(t_1, t_2) dt_1 dt_2 \\ &\quad + \iint_{D_2} R_{11}(t_2, t_1) R_{22}^*(t_2, t_1) dt_1 dt_2 \end{aligned} \quad (\text{B.3})$$

for D_1 and D_2 the regions of integration for each integral, as depicted in Fig. 30. The bottom line of (B.3) comes from the conjugate symmetry property in (B.2).

Imposing the limits of integration per Fig. 30 then yields

$$\begin{aligned} & \langle R_{22}(t_1, t_2), R_{11}(t_1, t_2) \rangle_{t_1, t_2} \\ &= \int_0^T \int_0^{t_2} R_{11}^*(t_1, t_2) R_{22}(t_1, t_2) dt_1 dt_2 \\ &\quad + \int_0^T \int_{t_2}^T R_{11}(t_2, t_1) R_{22}^*(t_2, t_1) dt_1 dt_2 \\ &= \int_0^T \int_0^{t_2} R_{11}^*(t_1, t_2) R_{22}(t_1, t_2) dt_1 dt_2 \\ &\quad + \left(\int_0^T \int_{t_2}^T R_{11}^*(t_2, t_1) R_{22}(t_2, t_1) dt_1 dt_2 \right)^*. \end{aligned} \quad (\text{B.4})$$

Based on Fig. 30, we can rearrange the integrations for the second summand in (B.4) as

$$\begin{aligned} & \left(\int_0^T \int_t^T R_{11}^*(t_2, t_1) R_{22}(t_2, t_1) dt_1 dt_2 \right)^* \\ &= \left(\int_0^T \int_0^{t_1} R_{11}^*(t_2, t_1) R_{22}(t_2, t_1) dt_2 dt_1 \right)^*. \end{aligned} \quad (\text{B.5})$$

Substituting 0 into (B.3) results in

$$\begin{aligned} & \int_0^T \int_0^T R_{11}(t_1, t_2) R_{22}^*(t_1, t_2) dt_1 dt_2 \\ &= \int_0^T \int_0^{t_2} R_{11}^*(t_1, t_2) R_{22}(t_1, t_2) dt_1 dt_2 \\ &+ \left(\int_0^T \int_0^{t_1} R_{11}^*(t_2, t_1) R_{22}(t_2, t_1) dt_2 dt_1 \right)^* \\ &= 2\text{Re} \left\{ \int_0^T \int_0^{t_2} R_{11}^*(t_1, t_2) R_{22}(t_1, t_2) dt_1 dt_2 \right\} \end{aligned} \quad (\text{B.6})$$

which provides the purely real result that we expect for computation of μ_0^2 .

APPENDIX C SINC-FUNCTION APPROXIMATION TO DETERMINE CROSS CORRELATION LEVEL

Based on the inner product form of the cross correlation derived in Section II, it is possible to develop a useful rule of thumb for the cross correlation level. This process is leveraged to confirm the heuristic based on the inverse of the time–bandwidth product. Specifically, we approximate each autocorrelation by a surrogate function that is readily integrable in closed form. The interfering waveforms are taken to be FM, and the autocorrelation shape is approximated by a sinc function, where $\text{sinc}(x) = \sin(x)/x$, the justification for which comes from the observation that LFM waveforms exhibit sinc-like autocorrelation sidelobes while also exhibiting cross correlations that follow the inverse time–bandwidth trend.

For simplicity, the interfering waveforms are assumed to have equal time support, though in the unequal case, the time support for integration can simply be set to the minimum of the two pulsedwidths. Waveform 1 has frequency support on $f \in (f_1^-, f_1^+)$ yielding bandwidth $B_1 = f_1^+ - f_1^-$, corresponding to the limits of rectangular spectra. Likewise, the spectrum for waveform 2 is similarly defined on $f \in (f_2^-, f_2^+)$. Finally, it is assumed without loss of generality that the waveforms have some spectral overlap, defined by $f_1^- \leq f_2^- \leq f_1^+ \leq f_2^+$. This scenario is depicted in Fig. 31 that illustrates the relationships between the waveforms' spectral bounds, as well as their frequency overlap, which will be shown to determine the cross correlation level.

Using the sinc approximation, the respective autocorrelations become

$$R_{11}(\tau) = a_1^2 \text{sinc}(B_1 \tau) \exp(j2\pi f_1 \tau) \quad (\text{C.1})$$

and

$$R_{22}(\tau) = a_2^2 \text{sinc}(B_2 \tau) \exp(j2\pi f_2 \tau) \quad (\text{C.2})$$

for waveform amplitudes a_1 and a_2 . Noting that the limits of integration for the inner product in (B.6) are from 0 to the

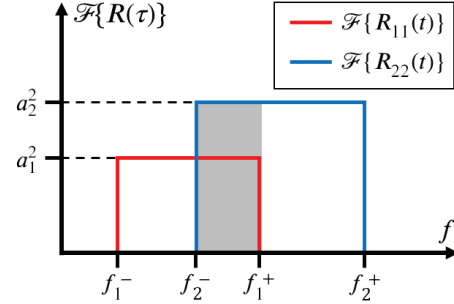


Fig. 31. Interfering radar spectra (rectangular support).

minimum pulsedwidth between the waveforms T , computation via (9) then yields

$$\begin{aligned} \mu_0^2 &= \frac{2}{E_1 E_2} \text{Re} \left\{ \int_0^T \int_0^v R_{11}^*(u) R_{22}(u) du dv \right\} \\ &= \frac{2a_1^2 a_2^2}{E_1 E_2} \int_0^T \int_0^v \left[\frac{\sin(\pi B_1 u)}{\pi B_1 u} \frac{\sin(\pi B_2 u)}{\pi B_2 u} \times \cos(2\pi(f_2^- - f_1^-)u) \right] du dv. \end{aligned} \quad (\text{C.3})$$

The steps to evaluate the double integral are omitted here, but (C.3) readily admits

$$\mu_0^2 = \frac{2a_1^2 a_2^2}{E_1 E_2} [A + B - C - D] \quad (\text{C.4})$$

where

$$A = \frac{1}{\beta} \begin{bmatrix} T \alpha_A \text{Si}(\alpha_A T) - 1 + \cos(\alpha_A T) \\ -\text{Ci}(\alpha_A T) + \ln(\alpha_A T) \end{bmatrix} \quad (\text{C.5a})$$

$$B = \frac{1}{\beta} \begin{bmatrix} T \alpha_B \text{Si}(\alpha_B T) - 1 + \cos(\alpha_B T) \\ -\text{Ci}(\alpha_B T) + \ln(\alpha_B T) \end{bmatrix} \quad (\text{C.5b})$$

$$C = \frac{1}{\beta} \begin{bmatrix} T \alpha_C \text{Si}(\alpha_C T) - 1 + \cos(\alpha_C T) \\ -\text{Ci}(\alpha_C T) + \ln(\alpha_C T) \end{bmatrix} \quad (\text{C.5c})$$

and

$$D = \frac{1}{\beta} \begin{bmatrix} T \alpha_D \text{Si}(\alpha_D T) - 1 + \cos(\alpha_D T) \\ -\text{Ci}(\alpha_D T) + \ln(\alpha_D T) \end{bmatrix} \quad (\text{C.5d})$$

for

$$\alpha_A = 2\pi(f_2^+ - f_1^-) \quad (\text{C.6a})$$

$$\alpha_B = 2\pi(f_1^+ - f_2^-) \quad (\text{C.6b})$$

$$\alpha_C = 2\pi(f_2^- - f_1^-) \quad (\text{C.6c})$$

$$\alpha_D = 2\pi(f_2^+ - f_1^+) \quad (\text{C.6d})$$

and

$$\beta = 4\pi^2 B_1 B_2. \quad (\text{C.6e})$$

The terms $\text{Si}(\cdot)$ and $\text{Ci}(\cdot)$ are the sine integral and cosine integral, respectively [32]. This expression can be simplified significantly by assuming that

$$|\alpha T \text{Si}(\alpha T)| \gg |1 - \cos(\alpha T) + \text{Ci}(\alpha T) - \ln(\alpha T)| \quad (\text{C.7})$$

which is true for even modest products $\alpha T \geq 10$. Similarly, given this assumption, $\text{Ci}(\alpha T) \approx 0$ and $\text{Si}(\alpha T) \approx (\pi/2)\text{sgn}(\alpha T)$. Inserting these simplifications into (C.4) results in

$$\mu_0^2 \approx \frac{2a_1^2 a_2^2}{E_1 E_2} \left[\frac{T \alpha_A}{\beta} + \frac{T \alpha_B}{\beta} - \frac{T \alpha_C}{\beta} - \frac{T \alpha_D}{\beta} \right]. \quad (\text{C.8})$$

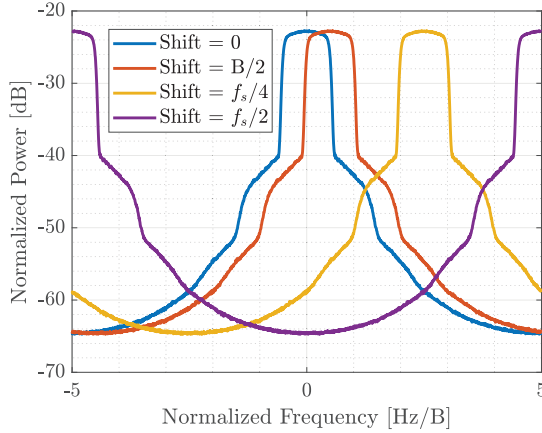


Fig. 32. Frequency-shifted super-Gaussian spectra (at baseband) to assess the impact of spectral roll-off on expected separability.

Subsequently, substituting in (C.6a)–(C.6e) yields

$$\mu_0^2 \approx \frac{T a_1^2 a_2^2}{B_1 B_2 E_1 E_2} [f_1^+ - f_2^-]. \quad (\text{C.9})$$

Noting that $E_1 = a_1^2 T$ and $E_2 = a_2^2 T$, (C.9) therefore becomes

$$\mu_0^2 \approx \frac{f_1^+ - f_2^-}{\text{TB}_1 \text{TB}_2} \quad (\text{C.10})$$

which directly relates the cross correlation power to the given bandwidths and their spectral overlap. Moreover, in the case of complete spectral overlap, where $B_1 = B_2$, $f_1^+ = f_2^+$, and $f_1^- = f_2^-$, (C.10) simplifies to

$$\mu_0^2 \approx \frac{1}{\text{TB}} \quad (\text{C.11})$$

which shows that, for the sinc approximation of autocorrelation, the mean square value of the cross correlation (at zero lag) is determined by the inverse of the mutual time-bandwidth product.

While (C.10) was derived assuming perfectly bandlimited waveforms, practical systems can at best achieve some degree of spectral containment that involves a reasonable roll-off. To assess the efficacy of (C.10) in the context of spectral roll-off, a baseband Monte Carlo simulation was performed using PRO-FM waveforms having $\text{TB} = 100$ and designed for a super-Gaussian spectral template [33]. The super-Gaussian template provides a convenient and practical means to control spectral containment via an exponent term that determines the ratio of energy contained in the 6-dB bandwidth (i.e., coinciding with swept bandwidth for LFM). Here, shape parameters of $p = 2, 4$, and 16 were used ($p = 2$ provides a Gaussian power spectrum, while higher p corresponds to increasingly rectangular spectra). As depicted in Fig. 32 for $p = 16$, the interfering waveform center frequency was shifted by varying degrees to evaluate the effect of the spectral roll-off on waveform separability.

For each frequency shift (and each super-Gaussian spectral template shape), 1000 cross correlation responses were generated from 1001 independent PRO-FM waveforms. The rms zero-lag cross correlation was then computed via (11) and plotted in Fig. 33. Noting that the normalized frequency axis is plotted in units of $[\text{Hz}/\text{B}]$ (meaning that a shift of 1 indicates

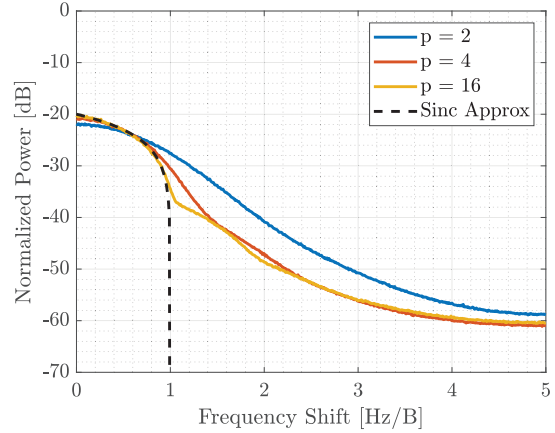


Fig. 33. RMS-averaged cross correlation between frequency-shifted waveforms obtained via Monte Carlo.

$f_1^+ = f_2^-$), it is interesting to observe that all three super-Gaussian shapes exhibit separability very close to the level predicted by (C.10) when the amount of normalized frequency shift is in the interval $[0, 1]$. Beyond a normalized frequency shift of 1, however, (C.10) yields a correlation of zero, while we clearly see a continued roll-off. This result indicates that (C.10), and likewise the inverse-TB rule, only applies when the passbands possess some degree of overlap.

APPENDIX D SINC BASIS EXPANSION

Consider some continuous time-domain signal $s(t)$ that we wish to describe by a discrete set of parameters denoted $\{\dots, s_{-2}, s_{-1}, s_0, s_1, s_2, \dots\}$. To do so, we can conveniently expand $s(t)$ via projection onto an orthonormal basis. Here, we choose the sinc basis since the resultant basis weights are simply the waveform samples, assuming a perfectly bandlimited waveform (clearly an approximation for pulsed radar). Thus, define the sinc basis expansion as

$$s(t) = \sum_{n=-\infty}^{\infty} s(nt_s) \text{sinc}\left(\frac{t}{T_s} - n\right) \quad (\text{D.1})$$

for discrete integer sample index n and sampling interval t_s . Truncating the summation limits to $n \in \{0, 1, \dots, N-1\}$ based on the time support T of $s(t)$, where $T = NT_s$, yields the finite-length signal vector $\mathbf{s} = [s_0, s_1, \dots, s_{N-1}]^\top$ for $s_n = s(nT_s)$. The basis expansion can then be written in the vector form as

$$s(t) \approx \sum_{n=0}^{N-1} s_n \text{sinc}\left(\frac{t}{T_s} - n\right) = \mathbf{p}^\top(t) \mathbf{s} \quad (\text{D.2})$$

where $\mathbf{p}(t) = [p_0(t), p_1(t), \dots, p_{N-1}(t)]^\top$ is the vector of sinc basis functions at time instant t , individually expressed as

$$p_n(t) = \text{sinc}\left(\frac{t}{T_s} - n\right). \quad (\text{D.3})$$

By using this basis expansion, a continuous-time waveform can be analyzed by a discrete set of parameters. This form is conveniently leveraged in Section IV, where the statistics of the samples of the normalized cross correlation are considered.

APPENDIX E MAXIMIZATION OF THE GUMBEL DISTRIBUTION

Here, we wish to solve for the maximum-likelihood estimates of the parameters μ and β in (40). To do so, the second-order Taylor expansion of (40) is computed and maximized in closed form. Since this procedure is most accurate when the Taylor expansion is performed near the peak of the likelihood function, the average maximum cross correlation is simulated via Monte Carlo, where the mutual time-bandwidth product is varied across several orders of magnitude. This approach allows for a reasonable Taylor expansion point to be reliably found, based only on waveform parameters (pulsewidth and bandwidth).

In general, a Gumbel random variable's likelihood function is better approximated by a 2nd-order Taylor expansion compared to its log-likelihood function. Since computing derivatives is simpler for the log-likelihood function, we first compute the derivatives of the log-likelihood function, which are then related to those of the standard likelihood function through the chain rule

Take the natural logarithm of (40) results in

$$\begin{aligned} L(\mu, \beta | \mathbf{x}) &= \sum_{k=0}^{K-1} \ln(P(\mu, \beta | X_k = x_k)) \\ &= -K \ln(\beta) - \sum_{k=0}^{K-1} \frac{x_k - \mu}{\beta} - \sum_{k=0}^{K-1} e^{-\frac{x_k - \mu}{\beta}} \end{aligned} \quad (\text{E.1})$$

so the first derivatives with respect to β and μ are

$$\frac{\partial L}{\partial \beta} = -\frac{1}{\beta} \left(K - \sum_{k=0}^{K-1} \frac{x_k - \mu}{\beta} \left(1 - e^{-\frac{x_k - \mu}{\beta}} \right) \right) \quad (\text{E.2})$$

and

$$\frac{\partial L}{\partial \mu} = \frac{1}{\beta} \left(K - \sum_{k=0}^{K-1} e^{-\frac{x_k - \mu}{\beta}} \right). \quad (\text{E.3})$$

The second derivatives of the log-likelihood function, representing elements of the Hessian matrix, are

$$\begin{aligned} \frac{\partial^2 L(\mathbf{x}; \mu, \beta)}{\partial \beta^2} &= \frac{1}{\beta^2} \left[K - \sum_{k=0}^{K-1} \left(\frac{2(x_k - \mu)}{\beta} \left(1 - e^{-\frac{x_k - \mu}{\beta}} \right) \right. \right. \\ &\quad \left. \left. + \left(\frac{x_k - \mu}{\beta} \right)^2 e^{-\frac{x_k - \mu}{\beta}} \right) \right] \end{aligned} \quad (\text{E.4a})$$

$$\frac{\partial^2 L(\mathbf{x}; \mu, \beta)}{\partial \beta \partial \mu} = -\frac{1}{\beta^2} \left(K - \sum_{k=0}^{K-1} e^{-\frac{x_k - \mu}{\beta}} \left(1 + \frac{x_k - \mu}{\beta} \right) \right) \quad (\text{E.4b})$$

$$\frac{\partial^2 L(\mathbf{x}; \mu, \beta)}{\partial \mu \partial \beta} = -\frac{1}{\beta^2} \left(K - \sum_{k=0}^{K-1} e^{-\frac{x_k - \mu}{\beta}} \left(1 + \frac{x_k - \mu}{\beta} \right) \right) \quad (\text{E.4c})$$

$$\frac{\partial^2 L(\mathbf{x}; \mu, \beta)}{\partial \mu^2} = \frac{1}{\beta^2} \sum_{k=0}^{K-1} e^{-\frac{x_k - \mu}{\beta}}. \quad (\text{E.4d})$$

Defining the vectors $\boldsymbol{\alpha} = [\mu, \beta]^T$ and $\boldsymbol{\alpha}_0 = [\mu_0, \beta_0]^T$, where $\boldsymbol{\alpha}_0$ is the point about which the Taylor expansion of (E.1) is performed, we can approximate the log-likelihood function as

$$T_L(\boldsymbol{\alpha}; \boldsymbol{\alpha}_0) = L(\boldsymbol{\alpha}_0 | \mathbf{x}) + (\boldsymbol{\alpha} - \boldsymbol{\alpha}_0)^T (\nabla_{\boldsymbol{\alpha}} L(\boldsymbol{\alpha}_0 | \mathbf{x}))$$

$$+ \frac{1}{2} (\boldsymbol{\alpha} - \boldsymbol{\alpha}_0)^T (\nabla_{\boldsymbol{\alpha}}^2 L(\boldsymbol{\alpha}_0 | \mathbf{x})) (\boldsymbol{\alpha} - \boldsymbol{\alpha}_0) \quad (\text{E.5})$$

which is quadratic in β and μ . To find the global maximum of (40), we first compute the gradient resulting in the linear equation

$$\nabla_{\boldsymbol{\alpha}} T_L(\boldsymbol{\alpha}; \boldsymbol{\alpha}_0) = \nabla_{\boldsymbol{\alpha}} L(\boldsymbol{\alpha}_0 | \mathbf{x}) + (\nabla_{\boldsymbol{\alpha}}^2 L(\boldsymbol{\alpha}_0 | \mathbf{x})) (\boldsymbol{\alpha} - \boldsymbol{\alpha}_0). \quad (\text{E.6})$$

The Taylor expansion of the actual likelihood function can be related to the expansion of the log-likelihood function using the chain rule via

$$\nabla P(\boldsymbol{\alpha}) = P(\boldsymbol{\alpha}) \nabla L(\boldsymbol{\alpha}) \quad (\text{E.7})$$

and

$$\nabla^2 P(\boldsymbol{\alpha}) = P(\boldsymbol{\alpha}) (\nabla_{\boldsymbol{\alpha}}^2 L(\boldsymbol{\alpha}) + \nabla_{\boldsymbol{\alpha}} L(\boldsymbol{\alpha}) \nabla_{\boldsymbol{\alpha}}^T L(\boldsymbol{\alpha})) \quad (\text{E.8})$$

where the notations $P(\boldsymbol{\alpha}) = P(\mu, \beta | \mathbf{x})$ and $L(\boldsymbol{\alpha}) = L(\mu, \beta | \mathbf{x})$ have been used for notational compactness. Inserting (E.7) and (E.8) into (E.6) then yields

$$\begin{aligned} T_P(\boldsymbol{\alpha}; \boldsymbol{\alpha}_0) &= P(\boldsymbol{\alpha}_0) [T_L(\boldsymbol{\alpha}; \boldsymbol{\alpha}_0) - L(\boldsymbol{\alpha}_0)] \\ &\quad + (\boldsymbol{\alpha} - \boldsymbol{\alpha}_0)^T \nabla_{\boldsymbol{\alpha}} L(\boldsymbol{\alpha}_0) \nabla_{\boldsymbol{\alpha}}^T L(\boldsymbol{\alpha}_0) (\boldsymbol{\alpha} - \boldsymbol{\alpha}_0) \end{aligned} \quad (\text{E.9})$$

with corresponding gradient

$$\begin{aligned} \nabla T_P(\boldsymbol{\alpha}; \boldsymbol{\alpha}_0) &= P(\boldsymbol{\alpha}_0) [\nabla T_L(\boldsymbol{\alpha}; \boldsymbol{\alpha}_0) \\ &\quad + 2 \nabla L(\boldsymbol{\alpha}_0) \nabla^T L(\boldsymbol{\alpha}_0) (\boldsymbol{\alpha} - \boldsymbol{\alpha}_0)]. \end{aligned} \quad (\text{E.10})$$

For convenience of presentation, define the normalized, data-dependent parameter $z_k = ((x_k - \mu_0)/\beta_0)$, and the following constants:

$$a_0 = \frac{1}{\beta_0} \sum_{k=0}^K (1 - e^{-z_k}) \quad (\text{E.11a})$$

$$a_1 = \frac{1}{\beta_0^2} \sum_{k=0}^K e^{-z_k} \quad (\text{E.11b})$$

$$a_2 = \frac{1}{\beta_0^2} \sum_{k=0}^K (1 - e^{-z_k})(1 - z_k) \quad (\text{E.11c})$$

$$b_0 = -\frac{1}{\beta_0} \sum_{k=0}^K (1 - z_k)(1 - e^{-z_k}) \quad (\text{E.11d})$$

$$b_1 = \frac{1}{\beta_0^2} \sum_{k=0}^K (1 - 2z_k)(1 - e^{-z_k}) + z_0^2 e^{-z_k}. \quad (\text{E.11e})$$

We can then rewrite the gradient of the Taylor expansion for the log-likelihood function in (E.10) in the form

$$\nabla T_L(\mu, \beta; \mu_0, \beta_0) = \begin{bmatrix} a_0 + a_1(\mu - \mu_0) + a_2(\beta - \beta_0) \\ b_0 + b_1(\beta - \beta_0) + a_2(\mu - \mu_0) \end{bmatrix} \quad (\text{E.12})$$

and the term from (E.10) used to compute the gradient for the full likelihood function can be written as

$$\begin{aligned} &2 \nabla L(\boldsymbol{\alpha}_0) \nabla^T L(\boldsymbol{\alpha}_0) (\boldsymbol{\alpha} - \boldsymbol{\alpha}_0) \\ &= 2((\mu - \mu_0)a_0 + (\beta - \beta_0)b_0) \begin{bmatrix} a_0 \\ b_0 \end{bmatrix} \\ &= \begin{bmatrix} 2a_0((\mu - \mu_0)a_0 + (\beta - \beta_0)b_0) \\ 2b_0((\mu - \mu_0)a_0 + (\beta - \beta_0)b_0) \end{bmatrix}. \end{aligned} \quad (\text{E.13})$$

Therefore, the gradient of the full, Taylor-expanded likelihood function becomes

$$\nabla T_p(\alpha; \alpha_0) = P(\alpha_0) \begin{bmatrix} \left\{ a_0 + (a_1 + 2a_0^2)(\mu - \mu_0) \right\} \\ \left\{ + (a_2 + 2a_0 b_0)(\beta - \beta_0) \right\} \\ \left\{ b_0 + (b_1 + 2b_0^2)(\beta - \beta_0) \right\} \\ \left\{ + (a_2 + 2a_0 b_0)(\mu - \mu_0) \right\} \end{bmatrix}. \quad (\text{E.14})$$

Setting (E.14) equal to zero and rearranging result in the system of linear equations

$$\begin{bmatrix} (a_1 + 2a_0^2) & (a_2 + 2a_0 b_0) \\ (a_2 + 2a_0 b_0) & (b_1 + 2b_0^2) \end{bmatrix} \begin{bmatrix} \mu - \mu_0 \\ \beta - \beta_0 \end{bmatrix} = - \begin{bmatrix} a_0 \\ b_0 \end{bmatrix} \quad (\text{E.15})$$

which can be used to solve for the vector parameter $[\mu - \mu_0, \beta - \beta_0]^T$ in terms of the data-dependent constants in (E.11a)–(E.11e). Doing so results in

$$\begin{bmatrix} (\mu - \mu_0) \\ (\beta - \beta_0) \end{bmatrix} = \frac{1}{D_0} \begin{bmatrix} -a_0(b_1 + 2b_0^2) + b_0(a_2 + 2a_0 b_0) \\ -b_0(a_1 + 2a_0^2) + a_0(a_2 + 2a_0 b_0) \end{bmatrix} \quad (\text{E.16})$$

where D_0 is the determinant of the matrix on the left-hand side of (E.15), that is,

$$D_0 = (a_1 + 2a_0^2)(b_1 + 2b_0^2) - (a_2 + 2a_0 b_0)^2. \quad (\text{E.17})$$

Based on (E.15), the maximum-likelihood parameter estimates for the Gumbel distribution are the location parameter

$$\hat{\mu}_{\text{ML}} \approx \mu_0 + \frac{-a_0(b_1 + 2b_0^2) + b_0(a_2 + 2a_0 b_0)}{(a_1 + 2a_0^2)(b_1 + 2b_0^2) - (a_2 + 2a_0 b_0)^2} \quad (\text{E.18})$$

and the corresponding scale parameter

$$\hat{\beta}_{\text{ML}} \approx \beta_0 + \frac{-b_0(a_1 + 2a_0^2) + a_0(a_2 + 2a_0 b_0)}{(a_1 + 2a_0^2)(b_1 + 2b_0^2) - (a_2 + 2a_0 b_0)^2}. \quad (\text{E.19})$$

It should be noted that the maximum-likelihood estimates for the parameters of the Gumbel distribution are still dependent on the data vector \mathbf{x} , meaning that data must be generated in order to estimate the maximum expected cross correlation values. To circumvent this dependence, now replace the data vector \mathbf{x} with its expected value $E\{\mathbf{x}\}$. The expected value for a Gumbel-distributed extreme value index x is

$$E\{x\} = \mu + \gamma\beta \quad (\text{E.20})$$

where $\gamma = 0.57721$ is the Euler–Mascheroni constant. For our purposes, the parameters μ and β are approximated by the Taylor expansion parameters μ_0 and β_0 that are found empirically. Note that this replacement implies that the Taylor expansion has been performed exactly at the maximum of the likelihood function. Thus, the variable z_k can be approximated as

$$z_k = \frac{x_k - \mu}{\beta} \approx \frac{(\mu_0 + \gamma\beta_0) - \mu_0}{\beta_0} = \gamma. \quad (\text{E.21})$$

Using (E.21), we can now approximate the data-dependent constants in (E.11a)–(E.11e) as

$$a_0 \approx \frac{K(1 - e^{-\gamma})}{\beta_0} \quad (\text{E.22a})$$

$$a_1 \approx \frac{Ke^{-\gamma}}{\beta_0^2} \quad (\text{E.22b})$$

$$a_2 \approx \frac{K(1 - e^{-\gamma}(1 - \gamma))}{\beta_0^2} \quad (\text{E.22c})$$

$$b_0 \approx -\frac{K(1 - \gamma(1 - e^{-\gamma}))}{\beta_0} \quad (\text{E.22d})$$

$$b_1 \approx \frac{K(1 - 2\gamma(1 - e^{-\gamma}) + \gamma^2 e^{-\gamma})}{\beta_0^2} \quad (\text{E.22e})$$

which are now independent of data vector \mathbf{x} . From this approximation, we can compute the limit of the maximum-likelihood estimates in (E.18) and (E.19) as K approaches infinity, for which $\lim_{K \rightarrow \infty} \hat{\mu}_{\text{ML}} = \mu_0$ and $\lim_{K \rightarrow \infty} \hat{\beta}_{\text{ML}} = \beta_0$. This result makes intuitive sense because the Taylor expansion was assumed to have been performed at the maximum of the likelihood function. In practice, we can never truly have an infinite number of data samples and typically only care about the maximum cross correlation on a per-pulse-pair basis. Consequently, we can simply set $K = 1$.

The final step to acquire a closed-form estimate for the maximum magnitude of the cross-filtered response is to choose the point $[\mu_0, \beta_0]$ where the Taylor expansion is performed. Here, the sample mean and sample variance are chosen to solve for the initial distribution parameters. Therefore, the Taylor-expanded procedure can be viewed as a refinement of the mean and variance estimation using the maximum-likelihood estimates of Gaussian distributed data.

To approximate the sample statistics for the maximum cross correlation between IID RFM waveforms, a Monte Carlo simulation was configured. Here, an ensemble of 2000 cross correlation functions were generated using uniformly distributed random PCFM waveforms, for each time–bandwidth product in the set $\text{TB} \in \{1, 2, \dots, 10^4\}$. The maximum values were computed for each correlation function, along with the sample average and variance. A log-domain least-squares regression was then performed assuming the model

$$\text{dB}[E\{M\}] = -c_1 \log_{10}(\text{TB}) + c_2 \quad (\text{E.23})$$

and

$$\text{dB}[\text{Var}\{M\}] = -c_3 \log_{10}(\text{TB}) + c_4 \quad (\text{E.24})$$

where c_1 – c_4 are the model constants to be determined through regression. For a given time–bandwidth product, let \mathbf{x} be the sample mean vector in dB and \mathbf{y} be the sample variance vector in dB. Also, let \mathbf{z} be the vector of log-domain inverse time–bandwidth products, that is, $z_i = -10 \log_{10}([\text{TB}]_i)$. The regression problem is solved by

$$\min_{c_1, c_2, c_3, c_4} \left\| \begin{bmatrix} c_1 & c_2 \\ c_3 & c_4 \end{bmatrix} \begin{bmatrix} \mathbf{z}^\text{T} \\ \mathbf{1}^\text{T} \end{bmatrix} - \begin{bmatrix} \mathbf{x} \\ \mathbf{y} \end{bmatrix} \right\|^2 \quad (\text{E.25})$$

which is quadratic and can therefore be solved in a closed form. For the specific dataset shown in Figs. 34 and 35, the regressed constants are presented in Table V.

Using the above regression constants, the Taylor expansion point can be solved as

$$\mu_0 = 10^{\frac{-c_1 \log(\text{TB}) + c_2}{20}} - \gamma\beta_0 \quad (\text{E.26})$$

and

$$\beta_0 = \left(\frac{\pi^2}{6} 10^{\frac{-c_3 \log(\text{TB}) + c_4}{10}} \right)^{\frac{1}{2}}. \quad (\text{E.27})$$

From these formulas and the regression constants given in Table V, an approximate but accurate maximum-likelihood

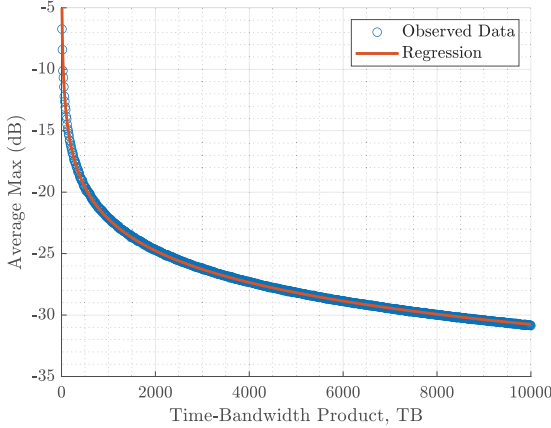


Fig. 34. Observed average cross correlation obtained via Monte Carlo simulation, compared to the implemented log-domain least-squares regression.

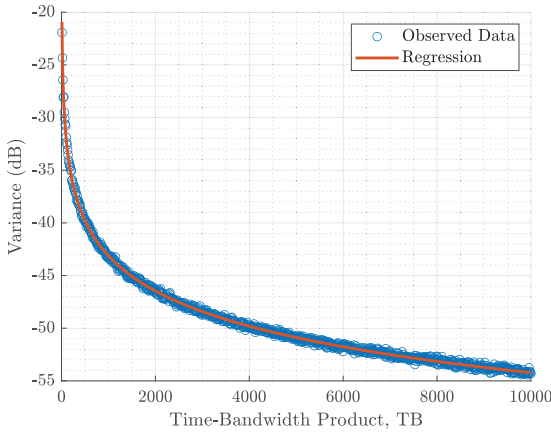


Fig. 35. Observed cross correlation variance obtained via Monte Carlo simulation, compared to the implemented log-domain least-squares regression.

TABLE V
REGRESSION CONSTANTS

c_1	0.85781
c_2	3.5402...
c_3	1.1107...
c_4	-9.8010...

estimate can be computed for the distribution parameters of the Gumbel distribution corresponding to two cross-correlating RFM waveforms using (E.18), (E.19), and (E.22a)–(E.22e).

It should be noted that the Taylor expansion, and subsequent regression, performed here specifically depends on the mutual time-bandwidth product and not the individual time-bandwidth products of the interfering waveforms. As such, the resulting predictors of the maximum cross correlation are generalizable for all independently generated RFM waveforms with a measurable degree of common time-frequency support. This result is validated in Section VI, where it is shown that the regression of (E.25) alone provides a good predictor of maximum cross correlation, with the Taylor-expanded maximum-likelihood estimates of (E.18) and (E.19) providing further refinement.

ACKNOWLEDGMENT

Distribution Statement A. Approved for Public Release.

Authorized licensed use limited to: UNIVERSITAS TELKOM. Downloaded on September 08, 2025 at 05:20:36 UTC from IEEE Xplore. Restrictions apply.

REFERENCES

- [1] S. D. Blunt and E. L. Mokole, “An overview of radar waveform diversity,” *IEEE Aerosp. Electron. Syst. Mag.*, vol. 31, no. 11, pp. 2–42, Nov. 2016.
- [2] M. B. Heintzelman, C. C. Jones, P. M. McCormick, and S. D. Blunt, “Mismatched complementary-on-receive filtering (MiCRFt) for MIMO radar,” in *Proc. IEEE Radar Conf. (RadarConf)*, Denver, CO, USA, May 2024, pp. 1–6.
- [3] X. Li, X. Wang, Q. Yang, and S. Fu, “Signal processing for TDM MIMO FMCW millimeter-wave radar sensors,” *IEEE Access*, vol. 9, pp. 167959–167971, 2021.
- [4] J. Ender and J. Klare, “System architectures and algorithms for radar imaging by MIMO-SAR,” in *Proc. IEEE Radar Conf.*, Pasadena, CA, USA, Jan. 2009, pp. 1–6.
- [5] D. Cohen, D. Cohen, and Y. C. Eldar, “High resolution FDMA MIMO radar,” *IEEE Trans. Aerosp. Electron. Syst.*, vol. 56, no. 4, pp. 2806–2822, Aug. 2020.
- [6] D. J. Rabideau, “Adaptive MIMO radar waveforms,” in *Proc. IEEE Radar Conf.*, Rome, Italy, May 2008, pp. 1–6.
- [7] N. Levanon and E. Mozeson, *Radar Signals*. Hoboken, NJ, USA: Wiley, 2004.
- [8] D. Sarwate, “Bounds on crosscorrelation and autocorrelation of sequences (Corresp.),” *IEEE Trans. Inf. Theory*, vol. IT-25, no. 6, pp. 720–724, Nov. 1979.
- [9] D. Sarwate and M. Pursley, “Crosscorrelation properties of pseudorandom and related sequences,” *Proc. IEEE*, vol. 68, no. 5, pp. 593–619, May 1980.
- [10] H. He, P. Stoica, and J. Li, “On aperiodic-correlation bounds,” *IEEE Signal Process. Lett.*, vol. 17, no. 3, pp. 253–256, Mar. 2010.
- [11] J. E. Stalder and C. R. Cahn, “Bounds for correlation peaks of periodic digital sequences,” *Proc. IEEE*, vol. 52, no. 10, pp. 1262–1263, Oct. 1964.
- [12] H. He, P. Stoica, and J. Li, “Designing unimodular sequence sets with good correlations—Including an application to MIMO radar,” *IEEE Trans. Signal Process.*, vol. 57, no. 11, pp. 4391–4405, Nov. 2009.
- [13] B. Liu, Z. He, J. Zeng, and B. Liu, “Polyphase orthogonal code design for MIMO radar systems,” in *Proc. CIE Int. Conf. Radar*, Shanghai, China, Oct. 2006, pp. 1–4.
- [14] M. Alaei-Kerahroodi, M. Modarres-Hashemi, and M. M. Naghsh, “Designing sets of binary sequences for MIMO radar systems,” *IEEE Trans. Signal Process.*, vol. 67, no. 13, pp. 3347–3360, Jul. 2019.
- [15] D. Shedd and D. Sarwate, “Construction of sequences with good correlation properties (Corresp.),” *IEEE Trans. Inf. Theory*, vol. IT-25, no. 1, pp. 94–97, Jan. 1979.
- [16] B. O’Donnell and J. M. Baden, “Fast gradient descent for multi-objective waveform design,” in *Proc. IEEE Radar Conf. (RadarConf)*, May 2016, pp. 1–5.
- [17] J. Song, P. Babu, and D. P. Palomar, “Sequence set design with good correlation properties via majorization-minimization,” *IEEE Trans. Signal Process.*, vol. 64, no. 11, pp. 2866–2879, Jun. 2016.
- [18] S. D. Blunt, M. Cook, J. Jakabosky, J. De Graaf, and E. Perriens, “Polyphase-coded FM (PCFM) radar waveforms, Part I: Implementation,” *IEEE Trans. Aerosp. Electron. Syst.*, vol. 50, no. 3, pp. 2218–2229, Jul. 2014.
- [19] S. D. Blunt, J. Jakabosky, M. Cook, J. Stiles, S. Seguin, and E. L. Mokole, “Polyphase-coded FM (PCFM) radar waveforms, Part II: Optimization,” *IEEE Trans. Aerosp. Electron. Syst.*, vol. 50, no. 3, pp. 2230–2241, Jul. 2014.
- [20] S. D. Blunt et al., “Principles and applications of random FM radar waveform design,” *IEEE Aerosp. Electron. Syst. Mag.*, vol. 35, no. 10, pp. 20–28, Oct. 2020.
- [21] C.-D. Chung and S.-M. Cho, “Constant-envelope orthogonal frequency division multiplexing modulation,” in *Proc. 5th Asia-Pacific Conf. 4th Optoelectron. Commun. Conf. Commun.*, Beijing, China, 1999, pp. 629–632.
- [22] S. C. Thompson, A. U. Ahmed, J. G. Proakis, J. R. Zeidler, and M. J. Geile, “Constant envelope OFDM,” *IEEE Trans. Commun.*, vol. 56, no. 8, pp. 1300–1312, Aug. 2008.
- [23] E. R. Biehl, C. A. Mohr, B. Ravenscroft, and S. D. Blunt, “Assessment of constant envelope OFDM as a class of random FM radar waveforms,” in *Proc. IEEE Radar Conf. (RadarConf)*, Florence, Italy, Sep. 2020, pp. 1–6.
- [24] J. Jakabosky, S. D. Blunt, and T. Higgins, “Ultra-low sidelobe waveform design via spectral shaping and LINC transmit architecture,” in *Proc. IEEE Radar Conf. (RadarCon)*, Washington, DC, USA, May 2015, pp. 1021–1026.

- [25] C. A. Mohr and S. D. Blunt, "Designing random FM radar waveforms with compact spectrum," in *Proc. ICASSP - IEEE Int. Conf. Acoust., Speech Signal Process. (ICASSP)*, Toronto, ON, Canada, Jun. 2021, pp. 8473–8477.
- [26] A. W. Doerry, "Generating nonlinear FM chirp waveforms for radar," Sandia, Albuquerque, NM, USA, Tech. Rep. SAND2006-5856, Sep. 2006.
- [27] P. Billingsley, *Probability and Measure*, 3rd ed., Hoboken, NJ, USA: Wiley, 1995.
- [28] M. H. DeGroot and M. J. Schervish, *Probability and Statistics*, 4th ed., London, U.K.: Pearson, 2012.
- [29] J. Beirlant, Y. Goegebeur, J. Teugels, J. Segers, D. De Waal, and C. Ferro, *Statistics of Extremes: Theory and Applications*. West Sussex, U.K.: Wiley, 2004.
- [30] P. Prescott and A. T. Walden, "Maximum likelihood estimation of the parameters of the generalized extreme-value distribution," *Biometrika*, vol. 67, no. 3, pp. 723–724, Dec. 1980.
- [31] L. Kocjancic, A. Balleri, and T. Merlet, "Study of the frequency slope effect on the chirp waveform orthogonality," in *Proc. Int. Conf. Radar Syst. (Radar)*, Belfast, U.K., Oct. 2017, pp. 1–6.
- [32] G. J. O. Jameson, "Sine, cosine and exponential integrals," *Math. Gazette*, vol. 99, no. 545, pp. 276–289, Jul. 2015.
- [33] M. B. Heintzelman, T. J. Kramer, and S. D. Blunt, "Experimental evaluation of super-Gaussian-shaped random FM waveforms," in *Proc. IEEE Radar Conf. (RadarConf)*, New York, NY, USA, Mar. 2022, pp. 1–6.

Matthew B. Heintzelman (Member, IEEE) received the B.S. and Ph.D. degrees in electrical engineering from the University of Kansas (KU), Lawrence, KS, USA, in 2019 and 2024, respectively.

He is now a Research Assistant Professor affiliated with the Radar Systems Laboratory, KU. He is author on two Journal papers and 14 peer-reviewed conference papers. During his Ph.D., he extensively studied waveform diversity and signal processing, specifically as applied to MIMO and multistatic radar systems. As a Researcher, he has developed a plethora of waveform optimization approaches, with a specific focus on hardware-implementable design, as well as novel signal processing algorithms aimed at mitigating multi-transmitter crosscorrelation interference. His research interests include radar signal processing, waveform diversity, design, and analysis, multistatic/MIMO radar, detection theory, and radar target tracking.

Dr. Heintzelman has competed as a top-5 finalist in the IEEE AESS student paper contest at the 2022 IEEE Radar Conference in New York City, NY.

Daniel B. Herr (Member, IEEE) received the dual Bachelor of Science degrees in electrical engineering and computer engineering from the Missouri University of Science and Technology, Rolla, MO, USA, in 2011, and the Ph.D. degree in electrical engineering from the University of Kansas (KU), Lawrence, KS, USA, in 2024.

He is currently a technical staff member at Massachusetts Institute of Technology (MIT) Lincoln Laboratory, Lexington, Massachusetts. His research focused on radar signal processing, waveform diversity, and estimation theory. His dissertation work explored the application of information-theoretic principles to the design of waveforms for pulse-agile radar operation. Prior to his Ph.D. studies, he worked as a Design Engineer at Garmin, Olathe, KS, from 2012 to 2018, designing avionics equipment that leveraged his electrical engineering expertise in the aerospace industry. His diverse background has equipped him with a unique perspective on the intersection of technology and radar systems.

Charles A. Mohr (Member, IEEE) received the B.S., M.S., and Ph.D. degrees from the University of Kansas, Lawrence, KS, USA, in 2016, 2019, and 2021, respectively.

He is currently a Research Assistant Professor with the University of Kansas and is affiliated with RSL/KARL. From August 2019 to June 2024, he worked at the Air Force Research Laboratory, Sensors Directorate, Wright-Patterson AFB, OH, USA as a Research Electronics Engineer. His research interests include radar waveform design, optimization theory, and digital signal processing. He has 17 refereed conference and journal publications as well as a patent.

Dr. Mohr was the recipient of second in the student paper conference at the 2019 IEEE radar conference.

Shannon D. Blunt (Fellow, IEEE) received the Ph.D. degree in electrical engineering from the University of Missouri (MU), Columbia, MO, USA, in 2002.

He is the Roy A. Roberts Distinguished Professor of Electrical Engineering and Computer Science (EECS) at the University of Kansas (KU), Director of the KU Radar Systems and Remote Sensing Laboratory (RSL), and Director of the Kansas Applied Research Laboratory (KARL). From 2002 to until 2005, he was with the Radar Division of the U.S. Naval Research Laboratory in Washington, D.C. He has over 200 refereed journal, conference, and book chapter publications, and 19 patents/patents-pending.

Dr. Blunt received an AFOSR Young Investigator Award in 2008, the IEEE/AESS Nathanson Memorial Radar Award in 2012, was named a Fellow of the IEEE in 2016, was appointed to the U.S. President's Council of Advisors on Science & Technology (PCAST) in 2019, received the 2020 IET Radar, Sonar & Navigation Premium Award, was named a Fellow of the Military Sensing Symposia (MSS) in 2024, and in 2025 received the IEEE/AESS Warren D. White Award as well as becoming the inaugural inductee in the MU EECS Alumni Hall of Fame. He coedited the books *Principles of Waveform Diversity & Design* (2010) and *Radar & Communication Spectrum Sharing* (2018). He has served as a subject matter expert on radar spectrum for DARPA, the Air Force's S&T 2030 Initiative, the National Spectrum Consortium, the Office of the Under Secretary of Defense for Research & Engineering (OUSD(R&E)), and the White House Office of Science & Technology Policy (OSTP). He served as Chair of the IEEE/AESS Radar Systems Panel and on the AESS Board of Governors. He is the Founding Editor-in-Chief for *IEEE TRANSACTIONS ON RADAR SYSTEMS*, served on the Editorial Board for *IET Radar, Sonar & Navigation*, and served in different editorial roles for *IEEE TRANSACTIONS ON AEROSPACE & ELECTRONIC SYSTEMS*. He has been General Chair or Technical Chair for multiple IEEE Radar Conferences and serves on the Program Committee for the MSS Tri-Service Radar Symposium series. He was also Chair of the NATO SET-179 research task group on "Dynamic Waveform Diversity & Design".

Cenk Sahin (Member, IEEE) received the B.S. degree in electrical and computer engineering from the University of Missouri - Kansas City, MO, USA, in 2008, and the M.S. and Ph.D. degrees in electrical engineering from the University of Kansas, Lawrence, KS, USA, in 2012 and 2015, respectively.

For his Ph.D. work he characterized channel coding and latency performance of various practical modulation schemes over wireless fading channels. As an NRC fellow at AFRL (2016-2018) he developed a family of spectrally-efficient constant-modulus radar-embedded communications waveforms. From 2018 to 2023, he was with the RF Technology Branch at the Sensors Directorate, Air Force Research Laboratory, WPAFB, OH where he led the design, development, and testing of spectrum-sharing methods for radar and communications, radar-embedded communication waveforms, and signal processing techniques for dual-function systems. Since May 2023, he has been with the Sensors Technologies Group, Air and Missile Defense Sector, Johns Hopkins University Applied Physics Laboratory. He is the author of seven journal papers, five (one issued, four pending) patents, 23 peer-reviewed conference papers, and two book chapters.

Dr. Sahin received the Richard K. & Wilma S. Moore Ph.D. Dissertation Award given to the best Ph.D. dissertation in the Department of Electrical Engineering & Computer Science, University of Kansas. In 2016, he was awarded the National Research Council (NRC) Postdoctoral Research Fellowship.

Andrew Kordik received the B.S. degree in computer engineering and the M.S. and Ph.D. degrees in electrical engineering from the University of Dayton, Dayton, OH, USA, in 2010, 2011, and 2023, respectively.

With over ten years of experience in the electrical and computing fields, he has focused on sensing and computing technologies. He has performed both independent research as well as lead teams in both the public and private sectors. In particular, he has an interest in the rapid development of advanced sensing capabilities, especially in combination with high performance and embedded computing solutions.